


Exploring two-dimensional coherent spectroscopy with exact diagonalization: Spinons and confinement in one-dimensional quantum magnets

Yoshito Watanabe ¹, Simon Trebst ¹ and Ciarán Hickey ^{2,3}

¹*Institute for Theoretical Physics, University of Cologne, 50937 Cologne, Germany*

²*School of Physics, University College Dublin, Belfield, Dublin 4, Ireland*

³*Centre for Quantum Engineering, Science, and Technology, University College Dublin, Dublin 4, Ireland*

 (Received 28 March 2024; revised 9 September 2024; accepted 8 October 2024; published 28 October 2024)

Two-dimensional coherent spectroscopy (2DCS) with terahertz radiation offers a promising new avenue for the exploration of many-body phenomena in quantum magnets. This includes the potential diagnosis of fractionalized excitations, for which linear response often struggles due to the indistinguishability of a continuum of fractional excitations from that caused by disorders or impurities. However, the interpretation of the complex results produced by 2DCS remains a challenge. Here, we explore a numerical approach based on exact diagonalization (ED) to help push forward our understanding of 2DCS and, as an example, use it to study the impact of confinement in the one-dimensional transverse field Ising (TFIM) model. We first validate our approach by comparing numerical ED and exact analytical results for the spectroscopic signatures of fractionalized spinons in the model, which exhibits a sharp spinon-echo signal in 2DCS, and show how to understand the finite-size effects inevitable with the inherently small system sizes in ED calculations. By augmenting the model with a longitudinal field, which breaks integrability and introduces confinement of spinon pairs, we observe significant changes to the 2DCS spectrum, such as nonsymmetric broadening of the spinon-echo signal. To further elucidate these changes, we introduce a “four-kink” approximation, an effective model that captures the interactions between multiple (confined) spinon pairs. Comparing ED data to these four-kink results provides understanding of the multiple features of the 2DCS spectra, allowing us to interpolate between finite-system size data and the thermodynamic limit. One advantage of our ED approach is its possible extension to finite temperatures, which we explore using thermally pure quantum states and demonstrate how the intensity and spectroscopic patterns of 2DCS change when going beyond the integrable model. Our numerically exact results provide a benchmark for future experiments and theoretical studies relying on approximation methods and pave the way for the exploration of fractionalized excitations in quantum magnets.

DOI: [10.1103/PhysRevB.110.134443](https://doi.org/10.1103/PhysRevB.110.134443)

I. INTRODUCTION

Terahertz (THz) spectroscopy, in which an incident THz pulse is used to excite and probe the dynamics of a system, is widely employed in the study of quantum materials [1–4]. In particular, the THz range aligns well with the typical excitation energies of quantum magnets. The technique can be understood within the framework of linear response, providing information akin to the dynamical spin structure factor, but restricted to zero momentum. In conventional magnets, this form of linear response typically reveals sharp excitation modes, such as magnons or triplons. However, in systems with fractionalized excitations, linear response typically reveals a broad continuum of excitations, reflecting the underlying fact that local operators create multiple (deconfined) excitations [5–7]. Extracting meaningful information from the continuum is notoriously difficult, and distinguishing between a continuum arising from fractionalized excitations and one arising from, for example, thermal or impurity-induced disorder [8–12], presents a profound challenge to the field. This complexity highlights the need for complementary methods or approaches to accurately characterize dynamics in quantum materials, particularly in distinguishing the nuances of its excitation spectra.

A recently developed method to gain deeper insights into the dynamics of unconventional magnets is to expand THz spectroscopy to include *multiple* excitation pulses [13–15]. Using two THz pulses to probe the system and, in addition, varying the timing between the two pulses, leads to two-dimensional coherent spectroscopy (2DCS)—a technique that, in the optical range, has already been extensively used in fields such as quantum chemistry, to probe the structure of complex molecules [16], and semiconductor physics, to probe the dynamics of excitons [17]. At its heart, such a multi-pulse approach allows one to extract, by subtracting the single pulse responses from the multipulse response, the *non-linear* response of the system. This reveals the physics of higher-order dynamical correlation functions, inherently providing more information than that available with linear response. It can be analyzed either in the time domain, or, by performing a two-dimensional Fourier transform over the two time arguments, τ , the time delay between the two pulses, and t , the measurement time after the second pulse, in the frequency domain.

It is becoming increasingly clear that 2DCS with THz sources has the potential to become a potent new tool in exploring many-body phenomena in quantum magnets, such as in studying spin waves [13–15,18] or, more enticingly,

fractionalized quasiparticles such as spinons [19–24]. The latter example was first studied in Ref. [19], which showed that 2DCS can clearly identify one of the most elementary forms of fractionalized excitations—spinon excitations in the (exactly solvable) one-dimensional transverse field Ising model (1D-TFIM). A “spinon echo” signal, represented by a sharp antidiagonal line along the $\omega_t = -\omega_\tau$ direction, arises from the interference of phases accumulated by spinon pairs created by consecutive THz pulses. Weak perturbations, which introduce a finite lifetime to the spinon pairs, manifest as an energy-dependent broadening of the spinon echo signal, thereby revealing the lifetime of the individual spinon excitations [21,25]. However, the fate of the signal beyond the perturbative regime has not yet been explored.

Despite the enormous potential of 2DCS, the calculation of the relevant nonlinear response functions, and the interpretation of the 2DCS spectrum, is, in general, a challenging task. In the context of fractionalized excitations, other exactly solvable models, such as the toric code model [26] and Kitaev honeycomb model [27–29] have also been studied, as well as an analytical study exploring the potential for identifying fractional statistics [30]. Outside of exactly solvable models, or their perturbative regime, numerical studies have so far been restricted to the realm of matrix product states (MPS). There, two different approaches, either computing the full nonlinear magnetization [21], or directly computing the relevant susceptibility [22,23], have been demonstrated so far.

Here, we tackle both of the above issues by, on the one hand, exploring the utility of using exact diagonalization (ED) to study 2DCS and, on the other hand, using ED to study the impact of confinement on the characteristic spinon-echo signal of the 1D-TFIM. ED is well-suited to achieving long-time evolution, and correspondingly high-frequency resolution, but it is obviously rather limited in terms of system sizes. As such, it offers a different numerical trade-off than recent exploratory studies [21,22] using MPS time evolution, which can deal with much larger system sizes than ED but can be limited to shorter time scales due to the growth of entanglement under time evolution [31]. To showcase the applicability of our ED approach, we consider the 1D-TFIM and critically discuss finite-size effects in its exactly solvable limit and then extend our study to the case where the integrability is broken by a longitudinal field, introducing a confining potential for the spinon excitations. We demonstrate that the fine resolution in the frequency domain achieved by ED reveals a detailed structure of the 2DCS spectrum characterized by a sequence of interacting spinon-pair bound states. Of particular interest is the evolution of the spinon-echo signal, a key signature of fractionalized excitations in the (exactly solvable) 1D-TFIM. By applying both ED on the full model, and using an effective four-kink approximation that allows us to access large system sizes, we identify that the significant changes in the spinon-echo signal result from the interacting nature of spinon pairs as well as field-induced breaking of spinon bound states into pairs of lower-energy bound states. Finally, we extend our approach to finite temperatures, a crucial development for comparison with future experiments.

Our discussion in the following is structured as follows. We start, in Sec. II, with a general overview of 2DCS, details on how we numerically compute the associated nonlinear

response functions with ED, and the model Hamiltonian that we focus on in this work. Next, in Sec. III, we investigate the origin of finite-size effects in the 1D-TFIM and discuss how to interpret the resulting 2DCS spectra. With the understanding of the finite-size effects in hand, we then turn to the case of a longitudinal field in Sec. IV. Combining our ED results with a “four-kink” approximation, we show the confinement of spinon pairs results in a significant change of the “spinon-echo” signal. Finally, in Sec. V, we discuss the ED approach to finite temperatures and demonstrate how the finite-temperature effects can be captured in 2DCS. In Sec. VI, we summarize our results and discuss the experimental relevance of our findings.

II. METHODS

Before discussing any results, we first provide a brief overview of magnetic 2DCS and its theoretical underpinnings, details on how we numerically compute the associated nonlinear response functions with ED, and the model Hamiltonian that we focus on in this work.

A. Formalism of 2DCS

We consider a simple time-dependent magnetic field consisting of two δ -function pulses at times $t' = 0$ and $t' = \tau$. The magnetization is measured after the second pulse at a time $t' = t + \tau$. Thus τ is the delay time between the two pulses and t is the measurement time after the second pulse. The α component of the resulting time-dependent applied field can be written as $B^\alpha(t') = B_0^\alpha \delta(t') + B_\tau^\alpha \delta(t' - \tau)$.

We define $m_{0\tau}^\alpha(t, \tau)$ as the α component of the induced magnetization at time $t' = t + \tau$ after two successive pulses at $t' = 0$ with strength B_0 and at $t' = \tau$ with strength B_τ . Analogously, $m_0^\alpha(t, \tau)$ and $m_\tau^\alpha(t, \tau)$ represent the induced magnetization after single pulses at $t' = 0$ with strength B_0 and at $t' = \tau$ with strength B_τ , respectively. Subtracting these single-pulse magnetization responses (m_0^α and m_τ^α) from the two-pulse magnetization $m_{0\tau}^\alpha$ isolates the nonlinear magnetization as

$$\begin{aligned} m_{\text{NL}}^\alpha(t, \tau) &= m_{0\tau}^\alpha(t, \tau) - [m_0^\alpha(t, \tau) + m_\tau^\alpha(t, \tau)] \\ &= \chi_{\alpha\beta\gamma}^{(2)}(t, \tau) B_\tau^\beta B_0^\gamma + \chi_{\alpha\beta\gamma}^{(3)}(t, \tau, 0) B_\tau^\beta B_0^\beta B_0^\gamma \\ &\quad + \chi_{\alpha\beta\gamma}^{(3)}(t, 0, \tau) B_\tau^\beta B_\tau^\beta B_0^\gamma + \dots, \end{aligned} \quad (1)$$

wherein only mixed cross-terms survive (for example, second-order terms proportional to B_0^2 and B_τ^2 cancel out). This setup is schematically illustrated in Fig. 1. Note that, in this two-pulse setup, there is a single second-order susceptibility but two distinct third-order contributions proportional to $B_\tau B_0^2$ and $B_\tau^2 B_0$, respectively.

Concrete expressions for the nonlinear susceptibilities can be derived using time-dependent perturbation theory [32]. In general, they are written as the equilibrium expectation value of nested commutators of the magnetization operators. As an example, the relevant third-order susceptibility can be neatly expressed in its most general form as

$$\chi_{\alpha\beta\gamma\delta}^{(3)}(t_3, t_2, t_1) = \frac{2}{N} \text{Im}[R_1 + R_2 + R_3 + R_4], \quad (2)$$

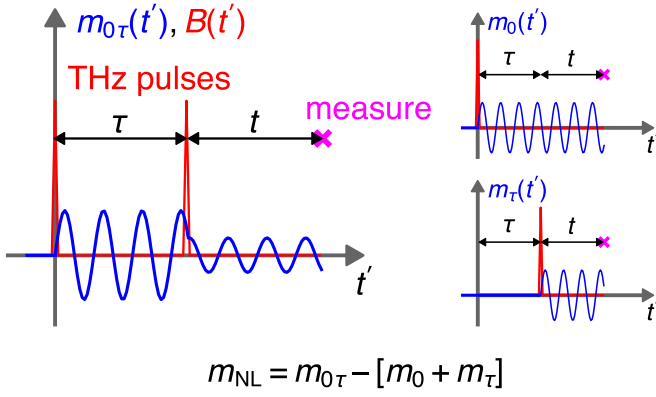


FIG. 1. Schematic of the two-pulse measurement setup. Two THz pulses (in red) are applied at times $t' = 0$ and $t' = \tau$, and the magnetization $m_{0\tau}$ (in blue) is measured at $t' = t + \tau$. Subtracting the single pulse responses, m_0 and m_τ , from $m_{0\tau}$ isolates the nonlinear magnetization m_{NL} .

where t_1, t_2 , and t_3 are the time delays for a general multipulse setup, and the R_a encode the contributions from the different possible orderings of the operators (we have suppressed their arguments and labels here for simplicity) given by

$$\begin{aligned} R_1 &= \langle M^\gamma(t_1) M^\beta(t_2 + t_1) M^\alpha(t_3 + t_2 + t_1) M^\delta(0) \rangle, \\ R_2 &= \langle M^\delta(0) M^\beta(t_2 + t_1) M^\alpha(t_3 + t_2 + t_1) M^\gamma(t_1) \rangle, \\ R_3 &= \langle M^\delta(0) M^\gamma(t_1) M^\alpha(t_3 + t_2 + t_1) M^\beta(t_2 + t_1) \rangle, \\ R_4 &= \langle M^\alpha(t_3 + t_2 + t_1) M^\beta(t_2 + t_1) M^\gamma(t_1) M^\delta(0) \rangle, \end{aligned} \quad (3)$$

where $M^\alpha(t) = \sum_i S_i^\alpha(t)$ and $S_i^\alpha(t)$ is the α component of the spin operator on site i at time t . By inserting resolutions of the identity, each R_a can be rewritten in terms of the energy eigenstates $|P\rangle, |Q\rangle$, and $|R\rangle$ as

$$\begin{aligned} R_1 &= \sum_{PQR} m_{0R}^\gamma m_{RQ}^\beta m_{QP}^\alpha m_{P0}^\delta e^{-iE_P t_1} e^{-i(E_P - E_R) t_2} e^{-i(E_P - E_Q) t_3}, \\ R_2 &= \sum_{PQR} m_{0R}^\delta m_{RQ}^\beta m_{QP}^\alpha m_{P0}^\gamma e^{+iE_R t_1} e^{-i(E_P - E_R) t_2} e^{-i(E_P - E_Q) t_3}, \\ R_3 &= \sum_{PQR} m_{0R}^\delta m_{RQ}^\gamma m_{QP}^\alpha m_{P0}^\beta e^{+iE_R t_1} e^{+iE_Q t_2} e^{-i(E_P - E_Q) t_3}, \\ R_4 &= \sum_{PQR} m_{0R}^\alpha m_{RQ}^\beta m_{QP}^\gamma m_{P0}^\delta e^{-iE_P t_1} e^{-iE_Q t_2} e^{-iE_R t_3}, \end{aligned} \quad (4)$$

where we have defined the magnetization matrix elements $m_{fi}^\alpha = \langle f | M^\alpha | i \rangle$. See Appendix A for the full expressions for $\chi^{(2)}$ and $\chi^{(3)}$ and their associated R_a .

Setting $t_1 = 0$, $t_2 = \tau$, $t_3 = t$ and $t_1 = \tau$, $t_2 = 0$, $t_3 = t$ yields $\chi_{\alpha\beta\gamma\gamma}^{(3)}(t, \tau, 0)$ and $\chi_{\alpha\alpha\beta\gamma}^{(3)}(t, 0, \tau)$ respectively. The two-dimensional Fourier transform of $\chi^{(3)}$ over positive t and τ generates the 2DCS frequency spectrum. We define $\chi^{(3;1)}(\omega_t, \omega_\tau) \equiv \text{FT}[\theta(t)\theta(\tau)\chi^{(3)}(t, \tau, 0)]$ and $\chi^{(3;2)}(\omega_t, \omega_\tau) \equiv \text{FT}[\theta(t)\theta(\tau)\chi^{(3)}(t, 0, \tau)]$. It is important to note here that the positive time constraint, $t > 0$, $\tau > 0$, imposed by the form $\theta(t)\theta(\tau)\chi(t, \tau)$, results in a convolution of $[\pi\delta(\omega_t) + 1/(i\omega_t)][\pi\delta(\omega_\tau) + 1/(i\omega_\tau)]$ with $\tilde{\chi}(\omega_t, \omega_\tau)$, where $\tilde{\chi}(\omega_t, \omega_\tau)$ is the unconstrained Fourier transform of

$\chi(t, \tau)$. Unfortunately, this convolution means that both the real and imaginary parts of the Fourier transform contain artificial broadening, e.g., an additional $1/(\omega_t\omega_\tau)$ term for the real part. This distortion of the spectrum of the pure $\tilde{\chi}(\omega_t, \omega_\tau)$ is commonly referred to as ‘‘phase twisting’’ [25,26] and is a known impediment to the clean interpretation of 2DCS spectra [16,33]. Nevertheless, we focus here only on $\text{Re}[\chi^{(2)}(\omega_t, \omega_\tau)]$ and $\text{Im}[\chi^{(3;1,2)}(\omega_t, \omega_\tau)]$. In the absence of the positive time constraint and if all matrix elements are real, these are the parts that would be nonvanishing.

B. Evaluation of nonlinear susceptibilities with exact diagonalization

We individually compute the nonlinear susceptibilities $\chi^{(2)}$ and $\chi^{(3)}$ using the approach developed in Ref. [21]. Similar to the experimental setup, this involves applying two Dirac- δ pulses to the system and analyzing the resulting time evolution to determine the nonlinear response. In the remainder, we focus on the case in which the field pulses and the measured magnetization are all aligned, so $\gamma = \beta = \alpha$. The action of a single pulse at time t' on a state $|\psi\rangle$ is described by

$$|\psi'\rangle = \exp(iB_{t'} M^\alpha) |\psi\rangle, \quad (5)$$

where $B_{t'}$ signifies the pulse magnitude. The wave function after two successive pulses, applied at times $t' = 0$ and τ is

$$|\psi(t, \tau)\rangle = e^{-iHt} e^{iB_\tau M^\alpha} e^{-iH\tau} e^{iB_0 M^\alpha} |\psi\rangle. \quad (6)$$

The magnetization per site after two successive pulses is thus given by

$$m^\alpha(t, \tau, B_\tau, B_0) = \frac{1}{N} \langle \psi(t, \tau) | M^\alpha | \psi(t, \tau) \rangle. \quad (7)$$

We can then calculate the individual nonlinear susceptibilities as follows:

$$\begin{aligned} \chi_{\alpha\alpha\alpha}^{(2)}(t, \tau) &= \left. \frac{\partial^2 m^\alpha(t, \tau, B_\tau, B_0)}{\partial B_\tau \partial B_0} \right|_{B_0=B_\tau=0}, \\ \chi_{\alpha\alpha\alpha\alpha}^{(3)}(t, \tau, 0) &= \left. \frac{\partial^3 m^\alpha(t, \tau, B_\tau, B_0)}{\partial B_\tau \partial B_0^2} \right|_{B_0=B_\tau=0}, \\ \chi_{\alpha\alpha\alpha\alpha}^{(3)}(t, 0, \tau) &= \left. \frac{\partial^3 m^\alpha(t, \tau, B_\tau, B_0)}{\partial B_\tau^2 \partial B_0} \right|_{B_0=B_\tau=0}. \end{aligned} \quad (8)$$

In practice, we numerically compute the derivatives using the central difference method. For example, $\chi_{\alpha\alpha\alpha}^{(2)}(t, \tau)$ can be computed using four different (B_0, B_τ) combinations. Setting $B_0 = B_\tau = B$, it can be written as

$$\begin{aligned} \chi_{\alpha\alpha\alpha}^{(2)}(t, \tau) &= \frac{1}{4B^2} [m^\alpha(t, \tau, B, B) - m^\alpha(t, \tau, -B, B) \\ &\quad - m^\alpha(t, \tau, B, -B) + m^\alpha(t, \tau, -B, -B)]. \end{aligned} \quad (9)$$

This method is similarly applied to the calculation of the third-order derivatives for $\chi_{\alpha\alpha\alpha\alpha}^{(3)}(t, \tau, 0)$ and $\chi_{\alpha\alpha\alpha\alpha}^{(3)}(t, 0, \tau)$, using six combinations of (B_0, B_τ) . Throughout, we use $B_0 = B_\tau = 0.001$. Note that one could alternatively directly compute the nonlinear susceptibilities via the R_a dynamical correlation functions, as given for example in Eq. (4) for $\chi^{(3)}$, for which the computational cost is comparable. One advantage of the present method is that, being closer to the actual experimental

setup, it allows for more flexibility and easier comparison to experimental results, e.g., one can easily take different pulse shapes, sequences and strengths into account in the time evolution, or even take the actual measured magnetic field pulse profile from an experiment and use that time-dependent magnetic field in the time evolution of Eq. (6).

To make the Fourier transform well-behaved with finite time windows, a filter function $e^{-\eta(t^2+\tau^2)}$ is applied, which broadens the signal in the frequency domain. We set a rather small broadening of $\eta = 0.001$, resulting in rather sharp peaks in the frequency domain. With this filter, we time evolve to a maximum time of $t_{\max} = \tau_{\max} = 150$. The sampling intervals δt and $\delta \tau$ determine the energy range as $\omega_t^{\max} = \pi/\delta t$ and $\omega_\tau^{\max} = \pi/\delta \tau$. We set $\delta t = \delta \tau = 0.25$. For the time evolution and application of the pulses, both of which are achieved by exponential operator multiplications, we use the package ‘‘Expokit.jl,’’ a JULIA implementation of EXPOKIT [34] that efficiently executes these calculations using Lanczos routines.

For the finite temperature simulations, we use the canonical thermal pure quantum state $|\phi\rangle = \exp(-\beta H/2)|\phi_0\rangle$ [35,36], where $|\phi_0\rangle$ is a random vector whose norm is initialized to one, as the initial state. We average the results over $N = 10$ random initial states. See Appendix B for the details of the finite temperature simulation.

C. 1D transverse field Ising model (1DTFIM)

The model we consider is the 1D-TFIM in the presence of a longitudinal field with the Hamiltonian

$$\mathcal{H} = -J \sum_{i=1}^L \sigma_i^z \sigma_{i+1}^z - h_x \sum_{i=1}^L \sigma_i^x - h_z \sum_{i=1}^L \sigma_i^z, \quad (10)$$

where σ_i^α ($\alpha = x, y, z$) are Pauli matrices at site i , $J > 0$ is the nearest neighbor ferromagnetic (FM) coupling, h_x is the transverse field, and h_z the longitudinal field. We assume periodic boundary conditions throughout. When $h_z = 0$, the model is exactly solvable via a Jordan-Wigner transformation, and, in the low-field ferromagnetically ordered phase, the elementary excitations are the kinks, or ‘‘spinons,’’ of the FM order (domain walls between blocks of aligned spins). These form a gapped dispersive band of excitations with energies λ_k . However, a single spin flip σ_i^x generates a pair of spinons, with equal and opposite momenta. This form of fractionalization results in a continuum response at zero momentum when probed within the linear response regime.

A finite longitudinal field h_z breaks the integrability of the model, and generates a confining potential for the spinon pairs. Though the model is no longer exactly solvable, the resulting dynamics can be well described by a ‘‘four-kink’’ approximation, in which an effective Hamiltonian acting within the subspace of two spinon states is constructed [37,38]. At large h_z , the spinons are tightly bound, and connect to the single spin-flip excitations of the high-field limit.

III. FINITE-SIZE EFFECTS

Since the available system sizes are limited in ED, we first need to have a solid understanding of potential finite-size effects. Here, we investigate finite size effects in two distinct scenarios, namely, (i) a magnetic field pulse creates a pair of

excitations, meaning that linear response exhibits a continuum of excitations, and (ii) a magnetic field pulse creates only single excitations, meaning that linear response exhibits a discrete set of excitation modes. We will see that finite-size effects are more significant in the former scenario.

A. Revival of signals

If a system of interest has a continuous spectrum at zero momentum, then simulating 2DCS with a finite system size can lead to a spurious ‘‘revival of signals’’ in the time domain. As a result, the Fourier-transformed signal in the frequency domain deviates from the true behavior expected in the thermodynamic limit. Here, we illustrate that the origin of this deviation is a combination of the discrete nature of the spectrum in finite-sized systems and the positive time constraint, $t > 0$, $\tau > 0$, enforced in the experimental setup.

In Ref. [19], the full 2DCS spectrum for the exactly solvable 1D-TFIM was obtained (see Appendix C for the derivation). The third-order susceptibility $\chi_{xxxx}^{(3)}$ reads

$$\chi_{xxxx}^{(3)}(t_3, t_2, t_1) = \frac{1}{L} \sum_{0 < k < \pi} [A_k^{(1)} + A_k^{(2)} + A_k^{(3)} + A_k^{(4)}], \quad (11)$$

where

$$\begin{aligned} A_k^{(1)} &= -8 \sin^2 \theta_k \cos^2 \theta_k \sin(2\lambda_k(t_3 + t_2 + t_1)), \\ A_k^{(2)} &= 8 \sin^2 \theta_k \cos^2 \theta_k \sin(2\lambda_k(t_2 + t_1)), \\ A_k^{(3)} &= -4 \sin^4 \theta_k \sin(2\lambda_k(t_3 + t_1)), \\ A_k^{(4)} &= -4 \sin^4 \theta_k \sin(2\lambda_k(t_3 - t_1)), \end{aligned} \quad (12)$$

with λ_k the single-spin energies, and the angle θ_k defined by $\tan \theta_k = (2J \sin k)/(2J \cos k - 2h_x)$.

Figure 2 compares the analytical and numerical $\chi_{xx}^{(1)}$ and $\chi_{xxxx}^{(3;1,2)}$ of the 1D-TFIM in the FM phase. The analytical data are obtained for a large system size of $L = 500$ using Eq. (12), representing the expected behavior in the thermodynamic limit, and the numerical data is obtained for $L = 24$ with ED. For the ED data, we checked that the error between the analytical result and the ED result for the same system size is less than 10^{-5} in the time domain data, and no apparent increasing trend is evident during the chosen time evolution window.

There are unsurprisingly a number of similarities between the two system sizes. In $\chi_{xxxx}^{(3;1)}$, there is a pump-probe (PP) signal along the ω_t axis at $(\omega_t, \omega_\tau) = (2\lambda_k, 0)$. In $\chi_{xxxx}^{(3;2)}$, there is an antidiagonal signal at $\omega_t = -\omega_\tau = 2\lambda_k$ corresponding to the ‘‘spinon-echo’’ or rephasing (R) signal, originating from $A_k^{(4)}$. For the smaller system size, the discrete nature of these signals simply results from the discreteness of the momentum k . This is most evident in the linear response $\chi_{xx}^{(1)}$, where the $L = 24$ system contains a visibly discrete set of $L/2$ peaks, corresponding to the $L/2$ allowed pairs of spinons with momenta k and $-k$, while the larger system size effectively has a continuum of excitations due to its much larger number of k points.

There are two obvious differences though between the two system sizes. In the time domain, there are periodic revivals of the signal in the small system size used for the ED that

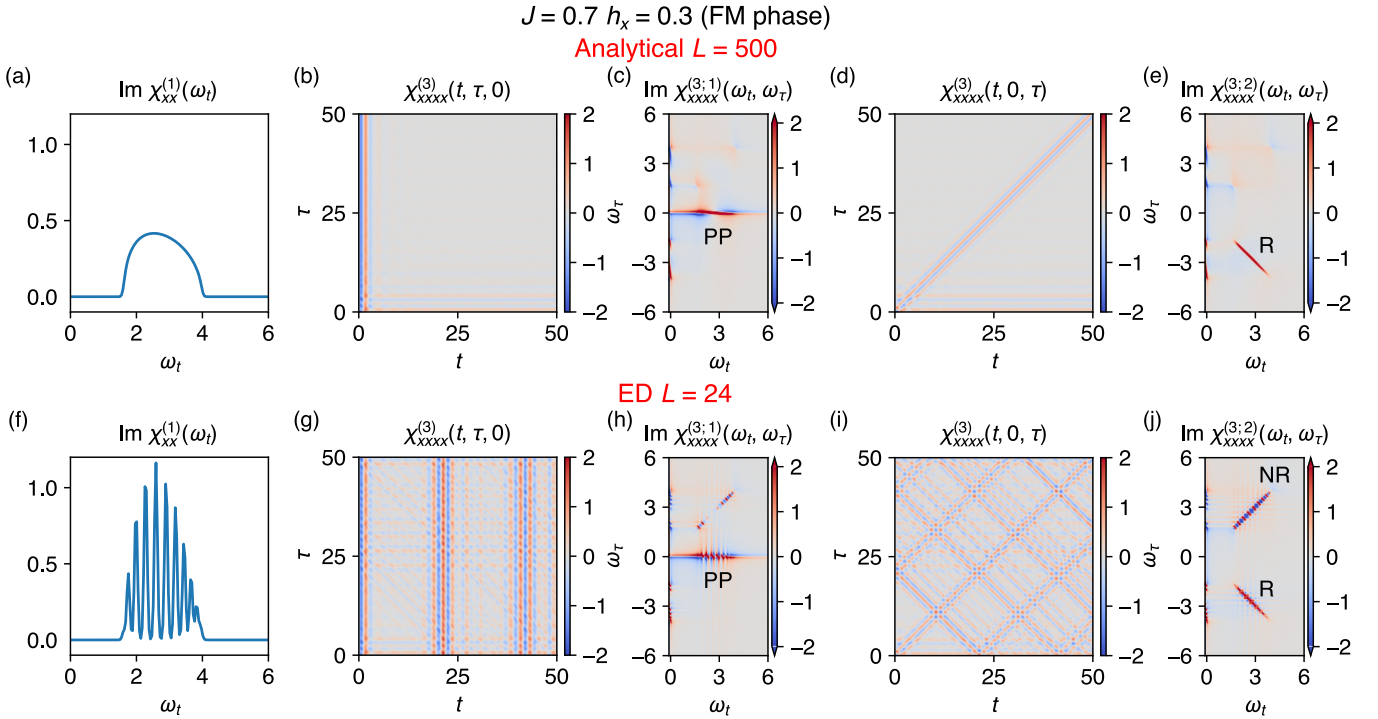


FIG. 2. Revival of the signal in the small system size in one-dimensional transverse field Ising (1D-TFIM). Two-dimensional coherent spectroscopy (2DCS) of 1D-TFIM with the model parameters $J = 0.7$, $h_x = 0.3$, i.e., ferromagnetic phase. [(a)–(e)] Analytically calculated linear-response $\text{Im}[\chi_{xx}^{(1)}(\omega_t)]$, third-order response $\chi_{xxxx}^{(3)}(t, t + \tau, t + \tau)$ and $\chi_{xxxx}^{(3)}(t, t, t + \tau)$ for $L = 500$, and 2d-FT of them. Spinon pairs manifest as continuous pump-probe (PP) signal at $\omega_\tau = 0$ in $\chi_{xxxx}^{(3;1)}$ and spinon-echo/rephasing (R) signal at $\omega_t = -\omega_\tau$ in $\chi_{xxxx}^{(3;2)}$. [(f)–(j)] The same quantities obtained by exact diagonalization (ED) for $L = 24$. Though the small t and τ data are similar to the that of large system size, the signal starts to revive as t and τ increase. The discrete character of the PP/R signal is evident. The nonrephasing (NR) signal at $\omega_t = \omega_\tau$ is also visible in $\chi_{xxxx}^{(3;2)}$, which is absent in the thermodynamic limit.

do not appear in the larger system size, and, in the frequency domain, there are additional diagonal nonrephasing (NR) signals in the small system size which are absent in the larger system size. To understand this, let's first consider a one-dimensional time domain, and for simplicity, assume that the energies of the spinons are equally spaced with a uniform frequency spacing of $\Delta\omega \propto 1/L$. If one superposes multiple sine waves, $\sum_{k>0} \sin(\omega_k t')$, with a uniform frequency spacing of $\Delta\omega$, then the wavelength of the resulting beating pattern will be proportional to $1/\Delta\omega$. In the thermodynamic limit, $L \rightarrow \infty$, $\Delta\omega \rightarrow 0$, and the spinon spectrum becomes continuous, which means that the wavelength diverges and the periodic signal disappears from the positive time axis, leaving a maxima at $t' = 0$.

In the two-dimensional time domain of relevance here, a similar scenario plays out. As illustrated in Fig. 3, for $L \rightarrow \infty$, we need to superpose a continuum of sine waves, $\int dk g(k) \sin[\omega_k(t \pm \tau)]$, with $g(k)$ simply representing matrix element factors. For the $t - \tau$ case, there is a maxima along the line $t = \tau$, and for the $t + \tau$ case, the maxima is along $t = -\tau$. Focusing on the relevant quadrant with $t > 0$, $\tau > 0$, only the $t = \tau$ line can be observed which, after Fourier transforming, is exactly the rephasing R signal. The $t = -\tau$ line is absent from the purely positive time window, and thus the absence of the corresponding nonrephasing NR signal is generally expected when the system has a continuous spectrum in the thermodynamic limit. On the other hand, for L finite, we are adding a finite number of frequencies,

$\sum_k g(k) \sin[\omega_k(t \pm \tau)]$, resulting in periodic signals with wavelengths roughly proportional to L . This means that, in the positive time quadrant, $t > 0$, $\tau > 0$, both rephasing and nonrephasing lines are present, and thus the Fourier transformed spectra have both signals present. The appearance of the NR signal is thus a consequence of the discreteness of the spectrum. In the ED, our time window for the FT in both t and τ extends to several times L , so we indeed observe both R and NR signals and, similarly, we are able to resolve the discrete nature of the signals.

It should be noted that there is a straightforward solution in this particular case to avoid such revivals of signals in the time domain. One can simply choose the time window small enough such that no revivals occur within it (alternatively, one can choose a large damping factor η in the filter function $e^{-\eta(t^2 + \tau^2)}$). Thus the NR signal will be absent and the R signal will be continuous, both as expected for the thermodynamic limit. For large system sizes, this is relatively straightforward as the periodic revivals are anyway spread far apart in time, but for the small system sizes accessible with ED this heavily constrains the available time window and hence leads to an extremely poor resolution in frequency space. More importantly, it is, in general, not possible to know *a priori* whether the revivals are an artifact, to be avoided, or a feature, to be included, i.e., whether the true physics is really a continuum or simply a dense set of discrete excitations (as, for example, observed in the confining scenario of the next section).

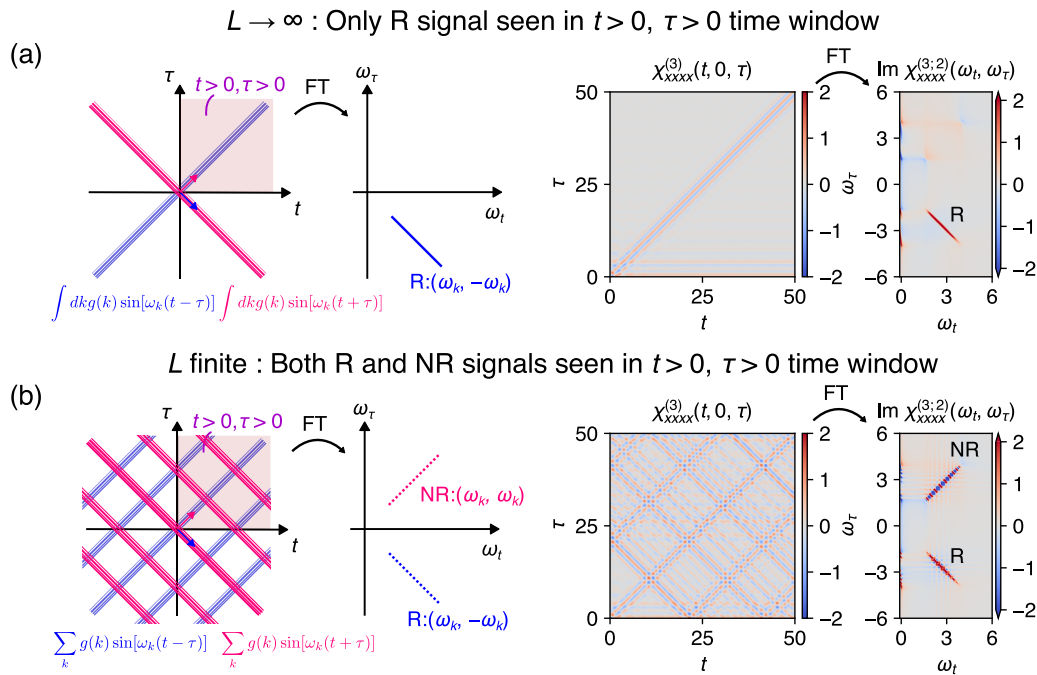


FIG. 3. Schematics of the rephasing (R) and nonrephasing (NR) signal. In the experiment, signals are measured at $t, \tau > 0$ represented by the shaded area. (a) In the thermodynamic limit, the signal can be described by a superposition of continuous poles; therefore, it takes the form of the integral. R signal decays as $t + \tau$ increases, and NR signal decays as $t - \tau$ increases. FT of the signal for $t, \tau > 0$ only reveals R signal. (b) In the finite size system, the signal takes the form of the sum due to the discrete nature of possible k . R and NR signals are visible at $t, \tau > 0$ as a revival of the signal. FT of the signal yields discrete R and NR signals.

In Fig. 3(a), it is the positive time constraint, $t > 0, \tau > 0$, that ensures that it is only the R signal that is present in the thermodynamic limit. If we were to include both positive and negative τ , then both the NR and R lines would be visible in the time domain, and hence one would observe both diagonal NR and antidiagonal R signals in the 2DCS spectrum. In addition, the artificial broadening induced by the positive time constraint in the Fourier transform would be absent (in the case of the imaginary part). Taken together, this means that, for the relaxed constraint, $t > 0$ only, the small system size ED result is simply a discretized version of the results in the thermodynamic limit, with all of the same qualitative features and signals (see Appendix D for an illustration of this).

Twisted Kitaev model

As another example in which identical finite size effects are present, we show results for another exactly solvable model, the twisted Kitaev model (TKM) [23,39–41]. The Hamiltonian is

$$\mathcal{H} = -J \sum_i^{L'} [\tilde{\sigma}_{2i-1}(\theta) \tilde{\sigma}_{2i}(\theta) + \tilde{\sigma}_{2i}(-\theta) \tilde{\sigma}_{2i+1}(-\theta)], \quad (13)$$

where $L' = L/2$, $\tilde{\sigma}_i(\theta) = \sigma_i^z \cos(\theta/2) + \sigma_i^y \sin(\theta/2)$, and θ is the “twist” angle. For $0 \leq \theta < \pi/4$, the ground state is a doubly degenerate FM state, polarized along the z direction. The elementary excitations are again spinons (kinks, or domain walls, of the FM state), but now there are two kinds of spinons, with dispersions l_k and λ_k , where $k = 2\pi n/L'$ and $n = 1, 3, \dots, L'$ [40].

Analytical expressions for the second- and third-order susceptibilities for the TKM have been derived in Ref. [23], with the result for $\chi_{xxxx}^{(3;2)}$ shown in Fig. 4(a) for a large system size of $L = 500$, again representing the behavior of the thermodynamic limit. Similar to the 1D-TFIM, a magnetic pulse along the x -direction only excites spinon pairs, with equal and opposite momenta; therefore there appears again a spinon-echo R signal. In addition, due to the interplay between the l_k spinons and λ_k spinons, there are additional streak features for both positive and negative ω_τ [40].

In ED, on an $L = 24$ chain, we observe all of the features of the analytical result in the thermodynamic limit, but with discretized streaks due to the discrete number of k points. Again, as in the TFIM, the main difference, in the frequency domain, is the additional diagonal NR signal, which is absent in the thermodynamic limit. The small system sizes available in ED are again able to capture the key qualitative features of the 2DCS spectrum, with the caveat that an additional NR signal presents itself.

B. Discrete spin-flip excitations in the paramagnetic phase

Next, we discuss finite size effects in the paramagnetic (PM) phase of the 1D-TFIM, i.e., $h_x > J$. In this phase, a magnetic field pulse along the z direction creates a single spin flip excitation with momentum $k = 0$, and the spectrum is expected to be discrete even in the thermodynamic limit. We thus expect that ED should be able to produce qualitatively similar results as those expected in the thermodynamic limit. Also, unlike the case of the FM ground state, we expect to observe an NR signal corresponding to single spin-flip excitations.

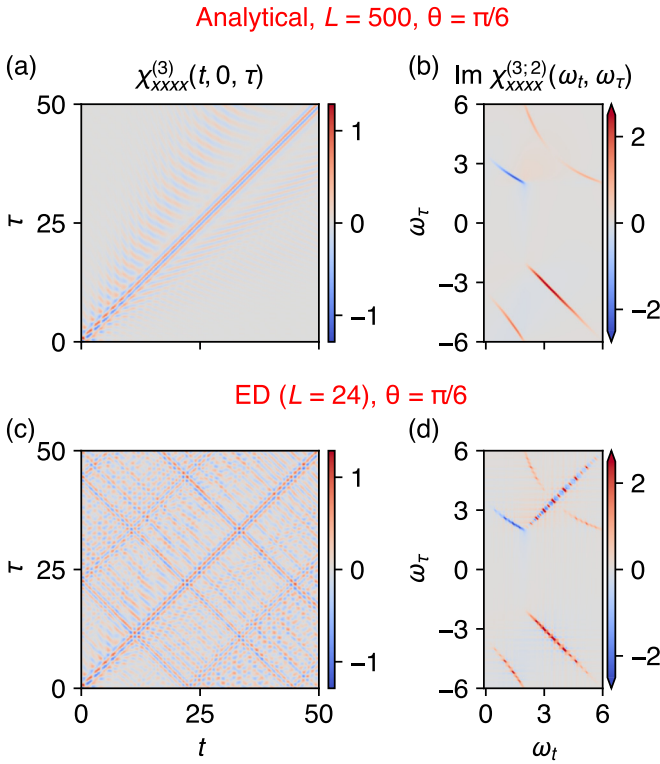


FIG. 4. Twisted Kitaev model. (a) Analytical result for $L = 500$. In addition to the R signal, there are streak features in both first and fourth quadrant, originating from the interplay between different spinon modes. (b) ED result for $L = 24$. Additional diagonal NR signal at $\omega_t = \omega_\tau$ is observed.

Figures 5(a) and 5(b) show $\chi^{(3;2)}$ for the trivial limit of $J = 0$, $h_x = 1$ ($h_x/J \rightarrow \infty$), in which the result can be obtained analytically. In this transverse field-only limit, the ground state can be written as $|0\rangle = |\rightarrow \rightarrow \dots \rightarrow\rangle$. Excitations involving either a single or double spin-flip at sites i or (i, j) are represented by $|\leftarrow\rangle_i = \sigma_i^z |0\rangle$ for a single site, and $|\leftarrow\rangle_i |\leftarrow\rangle_j = \sigma_i^z \sigma_j^z |0\rangle$ ($i \neq j$) for two sites, respectively. These are energy eigenstates with energies $E = 2h_x$ and $E = 4h_x$, respectively.

Keeping in mind that the matrix elements involved for $\chi^{(3)}$ can be written as $m_{0R}^z m_{RQ}^z m_{QP}^z m_{P0}^z$, we can think of two types of processes: one with $|Q\rangle = |0\rangle$, simplifying the matrix element to $|m_{0R}^z|^2 |m_{0P}^z|^2$, and another with $|Q\rangle$ involving double spin-flip states. In both cases, $|P\rangle$ and $|R\rangle$ are single spin-flip states. Noting that $(\sigma_i^z)^2$ is the identity operator, the number of contributions scales as L^2 for $|Q\rangle = |0\rangle$ processes, and as $2L(L-1)$ for processes with $|Q\rangle$ involving double spin-flip states. Combining these together, it can be shown that the summation of the different R_a in Eq. (2) for both types of processes results in a cancellation of the terms proportional to L^2 , leaving only the terms proportional to L . Dividing by L , we thus obtain system size-independent peaks at $(\omega_t, \omega_\tau) = (2h_x, 2h_x)$ and $(2h_x, -2h_x)$, corresponding to NR and R signals, respectively. Such a (partial) cancellation of terms proportional to L^2 is common and indeed will appear again in the next section. Note that unlike in the low-field FM phase, the NR signal does not vanish here as the pole is now discrete.

Analytical (thermodynamic limit), $J = 0$, $h_x = 1$

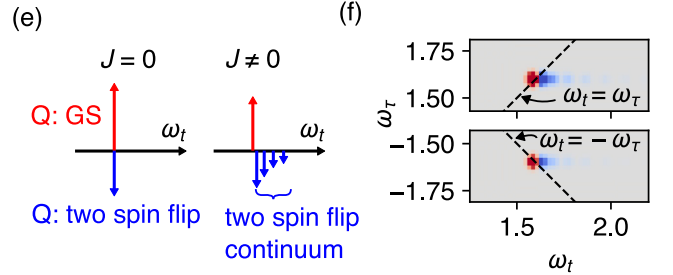
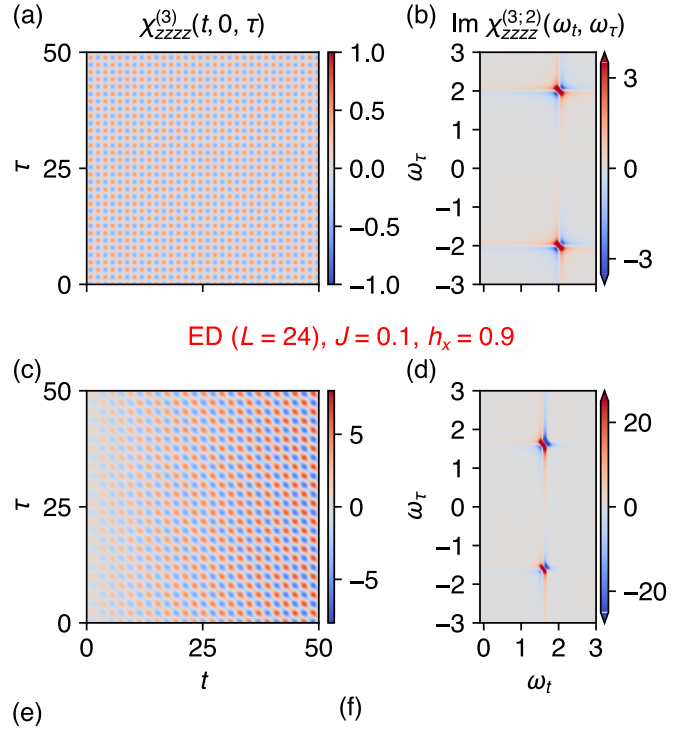


FIG. 5. Single spin flip excitations in paramagnetic phase (PM). [(a) and (b)] The result for $J = 0$, where the system size independent exact result is available. R and NR are observed at $(\omega_t, \omega_\tau) = (2h_x, -2h_x)$ and $(2h_x, 2h_x)$, respectively. [(c) and (d)] ED result for $L = 24$ with $J = 0.1$. (e) Schematics of the processes responsible for the NR signal. The intermediate state Q is either the ground states (red) or two-spin flip state (blue). In the presence of the interaction J , the two-spin flip states with zero total momentum constitute a continuum, which ends up with discrete poles in the finite size system. (f) Actual position of the poles for $L = 24$. The data are obtained by Fourier transforming both positive and negative time data, which eliminates the phase twisting effect. Slightly different frequencies of the signals with opposite signs are superposed, which manifests diverging behavior in the time domain data (c).

Next, we consider the effects of a finite Ising interaction J , by which the spin-flip excitation obtains a dispersion. Figures 5(c) and 5(d) show the ED result with $L = 24$ for $J = 0.1$ and $h_x = 0.9$. Similar to the noninteracting case, we observe NR and R signals at $(\omega_t, \omega_\tau) \approx (2h_x - 2J, 2h_x - 2J)$ and $(2h_x - 2J, -2h_x + 2J)$, respectively, whose energies corresponds to that of the single spin-flip excitation at $k = 0$. In the time domain data, the amplitude of the signal increases as t increases, see Fig. 5(c). Similar to the noninteracting case, the contribution from the processes with $|Q\rangle = |0\rangle$ should be partially canceled out by the processes with $|Q\rangle$ involving

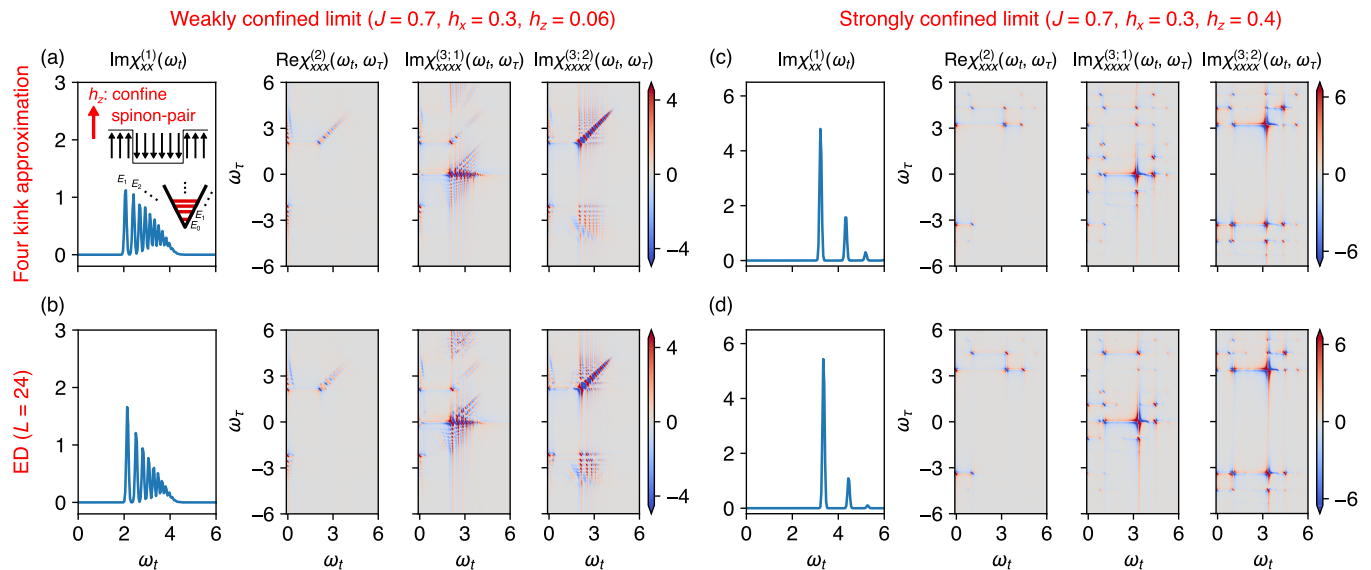


FIG. 6. Spinon-confinement via an applied longitudinal field with parameters $J = 0.7$, $h_x = 0.06$ in [(a) and (b)] the weakly confined limit, $h_z = 0.06$, and [(c) and (d)] the strongly confined limit, $h_z = 0.4$. All relevant susceptibilities, $\chi_{xx}^{(1)}$, $\chi_{xxx}^{(2)}$, and $\chi_{xxx}^{(3;1,2)}$ are shown. The results in [(a) and (c)] (top) are obtained using the four-kink approximation for a large system size ($L = 100$), while the results in [(b) and (d)] (bottom) are obtained with ED for $L = 24$.

two-spin flip states. However, since the double spin-flip states with $k = 0$ now form a continuum in the thermodynamic limit, this not only leads to the cancellation of the $|Q\rangle = |0\rangle$ processes, but also results in a tail of signals in the frequency domain [26,42,43], as schematically shown in Fig. 5(e). Indeed, in the zoomed in data of Fig. 5(f), both the numerical NR and R signals exhibit a tail in the frequency domain. The superposition of slightly different signal frequencies with opposite signs generates the diverging behavior in the time domain data, in line with the “long-time divergences” discussed in Ref. [18].

IV. BREAKING INTEGRABILITY AND CONFINEMENT

Having understood the impact of finite size effects, we now consider the addition of a longitudinal field, which introduces a confining potential for the spinon pairs. This explicitly breaks the integrability of the model, meaning it is no longer exactly solvable via a Jordan-Wigner transformation.

Though there is no longer an exact solution to compare the ED against, it is possible to numerically compute the response of large systems of $\mathcal{O}(100)$ sites using a few-kink approximation, derived by projecting the full Hamiltonian into the subspace of few-spinon states [37,38,44–46] (see Appendix E for details). Reference [22] explored the impact of confinement on the second-order response $\chi^{(2)}$ using a two-kink approximation. Here, we focus on $\chi^{(3)}$, and in particular the evolution of the spinon-echo rephasing signal, predicted as a key fingerprint of fractionalization [19], with increasing longitudinal field.

Figure 6 compares the *four-kink* approximation and ED results for $\chi_{xx}^{(1)}$, $\chi_{xxx}^{(2)}$, and $\chi_{xxx}^{(3;1,2)}$ for both the weakly confined, with $h_z = 0.06$, and strongly confined, with $h_z = 0.4$, cases. The confining potential leads to a set of spinon bound states with a discrete energy spectrum E_n (sometimes referred to

as “meson” bound states), clearly visible in the linear susceptibility $\chi_{xx}^{(1)}$. Intuitively, when the confinement potential is sufficiently strong, the n th excited state can be roughly associated with a domain of flipped spins (relative to the ground state) of length n . The energy spacing between these states increases as h_z increases, with for example only the lowest three visible within the frequency range $0 < \omega_t < 6$ in the strongly confined limit, $h_z = 0.4$. The second-order susceptibilities are consistent with Ref. [22] and are discussed in depth there.

In the weakly confined limit, $h_z = 0.06$, we see that even a small longitudinal field produces significant deviations from the integrable (zero confinement) results. First, in $\chi_{xxx}^{(3;1)}$, there is a series of additional features surrounding the on-axis pump-probe signal. More interestingly, in $\chi_{xxx}^{(3;2)}$, the spinon-echo R signal has now split into a grid of discrete peaks spread over a wide frequency range, accompanied by a set of weak line features shifted to $\omega_t < E_1$, in dramatic contrast to the single sharp antidiagonal line in the integrable case. We focus now on elucidating the origins of these new features and the evolution of the spinon-echo R signal (see also Appendix F for further details).

Firstly, the nature of the discrete grid of peaks occurring at energies $(\omega_t, \omega_\tau) = (E_n, -E_m)$ can be discerned by examining the structure of the Lehmann representation of the third-order response, as given in Eq. (4), with the relevant matrix elements involved being $m_{0R}^x m_{RQ}^x m_{QP}^x m_{P0}^x$. Similar to the PM phase discussed in Sec. III B, there are two distinct contributions to the peaks. In both cases, $|P\rangle$ and $|R\rangle$ are spinon bound states, but the intermediate state $|Q\rangle$ is different. In the first case, the intermediate state $|Q\rangle$ is the ground state and the $R_{2,3}$ process generates a grid of rephasing peaks with intensities proportional to $|m_{n0}^x|^2 |m_{m0}^x|^2$, with $n = m$ corresponding to the peaks on the diagonal and $n \neq m$ to peaks on the antidiagonal (see also Fig. 19 in Appendix G). This

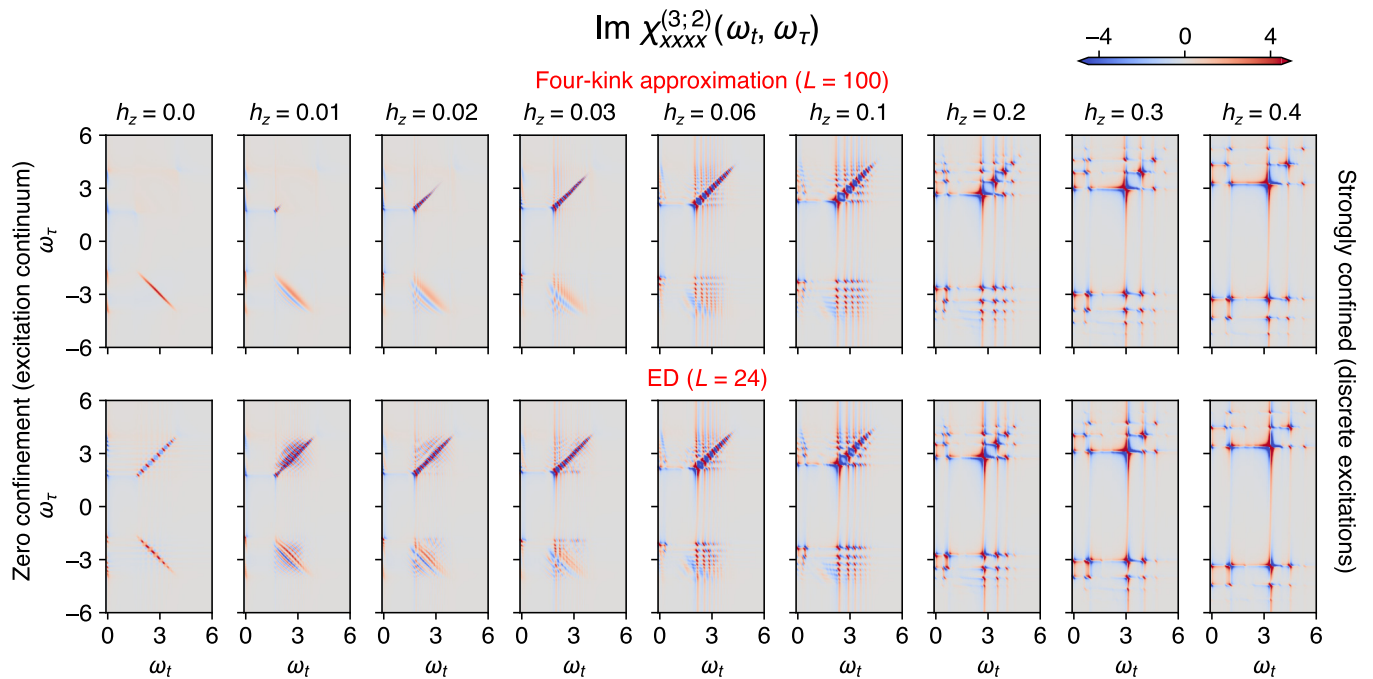


FIG. 7. Evolution of the spinon-echo rephasing signal. A comparison of $\chi_{xxxx}^{(3;2)}$, which contains the spinon-echo signal, for different longitudinal fields computed with the four-kink approximation (top) and ED (bottom). In both cases, the sharp spinon-echo signal at $h_z = 0$ is broadened as h_z increases, ending as a set of discrete peaks in the strongly confined regime.

contribution contains similar information to the linear response, as matrix elements of the form $|m_{n0}|^2 \propto L$ also appear there. The resulting matrix element is thus proportional to L^2 . As a result, this contribution to the third-order response is actually extensive, i.e., it scales with the system size L . This pathological behavior is remedied by taking the four-kink states into account as the intermediate state $|Q\rangle$. The four-kink states introduce cancellation terms, e.g., R_1 in $\chi_{xxxx}^{(3;2)}$ (see Fig. 19), regulating the apparent system size-dependent behavior, leading ultimately to L -independent signals. These remaining L -independent contributions, which survive the partial cancellation, reflect the interacting nature of the spinon-bound states. Note that, in addition to this grid of peaks, there is a continuum feature between each peak due to the four-kink states forming a continuum (more easily visible in Fig. 18 in Appendix F).

Secondly, the other prominent feature visible in the weakly confined limit is the series of predominantly negative line features appearing to the left of the R cross peaks at $(\omega_t, \omega_\tau) = (E_1, -E_n)$, where this negative signal appears only for $n \geq 3$. These features can be understood by considering processes in which a spinon bound pair breaks apart into two bound pairs of lower energy or, alternatively, a domain splits up into a pair of smaller domains. It is perhaps most straightforward to understand in the domain perspective. A domain of length n can be split into two smaller domains by flipping a spin somewhere within the domain, a process which requires n to be 3 or greater. The field pulses induce a domain splitting process, $(l = n) \rightarrow (l_1 = n - m - 1) + (l_2 = m)$, resulting in a pair of domains that form a continuum. One can also split a domain by flipping two spins, i.e., $(l = n) \rightarrow (l_1 = n - m - 2) + (l_2 = m)$, or by flipping three spins, and so on. This results in a series of line features of alternating sign (though only

the first three are clearly visible). Such processes account for the continuous signals appearing to the left of the rephasing peaks.

In the strongly confined limit, $h_z = 0.4$, we see that the number of peaks visible has sharply reduced, primarily due to the increased spacing in energy between bound states. In $\chi_{xxxx}^{(3;2)}$, the peaks along the anti-diagonal, as well as their associated cross-peaks, again originate from the case where the ground state is the intermediate state $|Q\rangle = |0\rangle$ /four-kink states, and $|P\rangle$ and $|R\rangle$ are spinon bound states. On the other hand, the terahertz rectification (TR) peaks on, and just off, the ω_τ axis originate purely from processes in which the intermediate state is a two-kink state (see also Fig. 18).

It is important to note that here the discreteness of the spectrum is not a finite-size effect, as it was in the integrable FM phase, but rather it has a clear physical origin. Therefore the NR signals observed in $\chi_{xxxx}^{(3;1,2)}$ are expected to remain even in the thermodynamic limit. Indeed, the four-kink approximation results, which well reproduce the ED data, are computed for much larger system sizes of $\mathcal{O}(100)$, suggesting small finite-size effects. Thus, in this particular case, the appearance of a finite NR signal is a direct consequence of confinement converting the spinon continuum into a discrete set of spinon bound states.

In Fig. 7, we show the full evolution of $\chi_{xxxx}^{(3;2)}$ with increasing longitudinal field, computed both within the four-kink approximation and ED. The sharp line features of the zero field case, corresponding to free, deconfined spinon pairs, quickly decompose into a discrete set of peaks due to the confining potential. The rephasing signal decomposes into a grid pattern of discrete peaks, a nonrephasing signal appears with a similar grid of diagonal and cross peaks, and the terahertz rectification signal along the ω_τ axis also decomposes

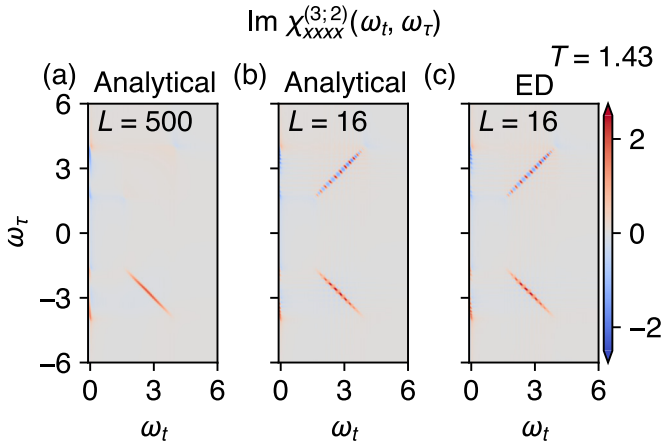


FIG. 8. Finite temperature spectra of 1D-TFIM. A comparison between analytical [(a) and (b)] and numerical (c) results of finite temperature with $L = 500$ and $L = 16$ is displayed. Parameters $J = 0.7$ and $h_x = 0.3$ are used for calculation.

into discrete peaks which expand along both directions in frequency space.

As $h_z \rightarrow 0$, the partial cancellation of the two processes responsible for the grid of R peaks becomes exact and, exactly at $h_z = 0$, only the sharp antidiagonal R signal remains. In addition, the features observed at $h_z = 0.06$, attributed to domain splitting processes, begin to merge to form an oscillating pattern with alternating signs on the lower left side of the antidiagonal R line as h_z decreases. The precise physical intuition behind this pattern, which has a clear picture at large h_z in terms of domains, close to the integrable limit still requires further study. As a result of the oscillating signal, in the four-kink approximation, the broadening of the R signal is asymmetric along $\omega_t = -\omega_\tau$, in contrast to the symmetric broadening caused by the finite lifetime of the spinon pairs [25].

V. FINITE TEMPERATURE

Finally, we make use of one of the other advantages of ED and extend our study to finite temperatures. As in the zero-temperature case, we first investigate the exactly solvable case with $h_z = 0$. Figure 8 shows $\chi_{xxxx}^{(3;2)}$ calculated for $L = 500$ and $L = 16$ at a temperature $T = 1.43$. For this model, one should note that this particular response function is rather special as the only change with temperature is in the intensities of the signals. For $L = 500$, the overall peak intensity is suppressed as temperature increases, but the rephasing R signal remains sharp in the two-dimensional frequency space. For $L = 16$, there are twice as many peaks in the signal, which is due to the fact that at finite temperatures we also have a contribution from the parity odd sector of the Jordan-Wigner transformed fermionic Hamiltonian of the TFIM model (see Appendix C for details). Similar to the zero-temperature case, we also observe a nonrephasing NR signal due to the finite system size, and no other additional signal appears. Figure 8(c) shows ED result for $L = 16$ at $T = 1.43$. The quantitative agreement between the analytical and ED results helps to validate our method for finite temperature.

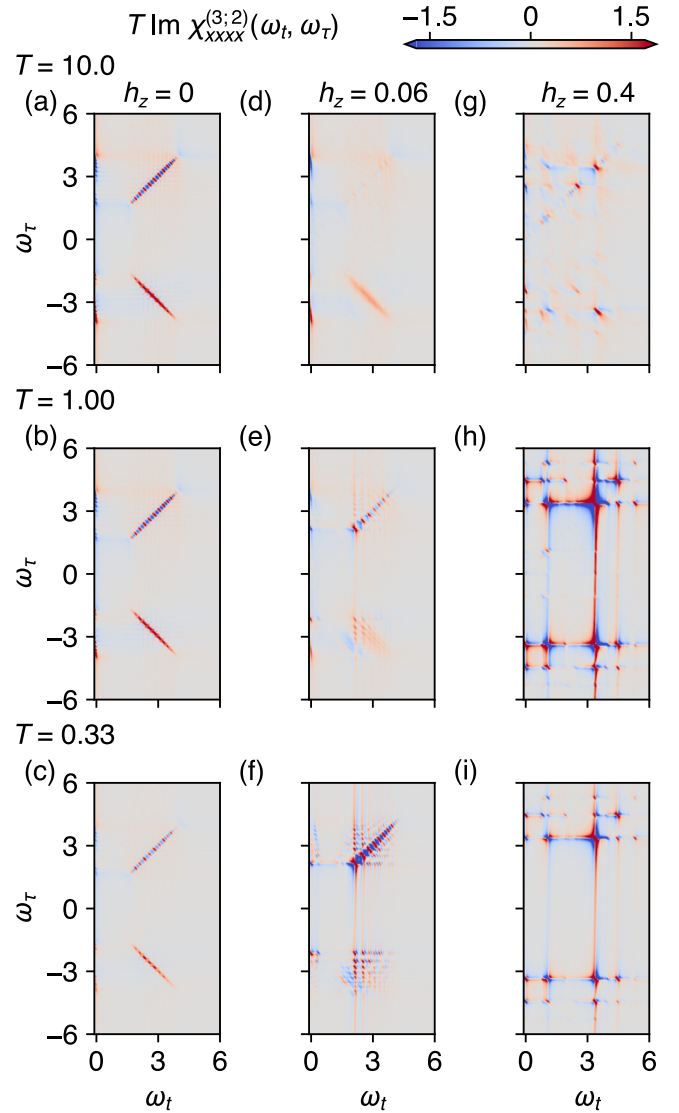


FIG. 9. Temperature dependence of $T \chi_{xxxx}^{(3;2)}(\omega_t, \omega_\tau)$ of the 1D-TFIM in a longitudinal field from ED. The parameters are $J = 0.7$ and $h_x = 0.3$. [(a)–(c)] $h_z = 0$, i.e., exactly solvable case with inverse temperature $T = 10.0, 1.00,$ and 0.33 , respectively. [(d)–(f)] $h_z = 0.06$. [(g)–(i)] $h_z = 0.4$.

Next, we investigate the finite-temperature 2DCS in the presence of the spinon confining potential. The impact on $\chi^{(3;2)}$ is shown in Fig. 9 for the zero, weakly, and strongly confined cases, with the data normalized by $\beta = 1/T$ so that they can be plotted with a common color scale. At a sufficiently low temperature of $T = 0.33$, which is below the specific heat peaks for all three cases (see Fig. 15 in Appendix B), the intensities and peak positions are close to the zero-temperature result. As temperature increases, the signal intensities decrease for all values of h_z . For the weakly confined case, $h_z = 0.06$, the discreteness of the low-temperature signal is smeared out as temperature increases, and the signal becomes continuous. In particular, at $T = 10.0$, the spectrum exhibits qualitative similarities to the $h_z = 0.00$ spectrum found in the thermodynamic limit, suggesting the impact of confinement can only be resolved at low temperatures. For $h_z = 0.4$, the

discreteness of the signal is preserved even at high temperatures. We also observe additional peaks along the line $\omega_t \approx 1$, which arise from the processes involving transitions between two-kink states.

VI. DISCUSSION

The calculation of nonlinear dynamical response functions for a quantum many-body system is a formidable and challenging task. We explored here, on the one hand, the utility of using ED to calculate nonlinear susceptibilities in the 1D-TFIM, and, on the other hand, the impact of confinement on the unique signatures of spinon fractionalization in the model. One of the key advantages of ED, the ability to simulate to long times without any corresponding increase in computational complexity, can be used to obtain high-resolution 2DCS spectra in frequency space. However, the key disadvantage, the relatively small system sizes available with ED, generates additional issues with interpreting the spectra due to potential finite size effects. We have discussed in detail these issues in the context of the 1D-TFIM and its two distinctive ground states. In both limits, ED can capture many of the important qualitative features expected, though care must be taken in distinguishing whether discrete excitations arise due to finite-size effects or due to some underlying physical mechanism. Using this knowledge, we were able to explore the impact of spinon confinement on the third-order susceptibilities, and, in particular, on the characteristic spinon-echo rephasing signal. Combining ED in small system sizes with the four-kink approximation in large system sizes, we were able to show how even a moderate longitudinal field can break up the sharp anti-diagonal signal and induce a visible nonrephasing signal.

In terms of experimental relevance, there are a number of materials whose dominant interactions can be written in the form of a 1D-TFIM. As an example, in CoNb_2O_6 , the FM chain of Co^{2+} ions is considered to be a good realization of the 1D-TFIM [37,38,41,47]. The dominant magnetic exchange interaction is an Ising interaction with an estimated $J=2.48$ meV $=0.6$ THz. The weak interchain interaction effectively introduces a longitudinal field, and the discrete spectrum of spinon bound states has been experimentally observed with linear response probes [37,38], including linear THz spectroscopy [41]. Therefore, with 2DCS, we would expect some qualitative features of the 2D spectrum computed here to also be observed in the material. However, it would be necessary to investigate the effects of additional terms, which are proposed to be relevant in the material, such as XY and bond-dependent interactions, in order to gain a quantitative understanding of the expected experimental spectrum.

An important caveat, relevant for any experimental comparison, is that in reality it is the nonlinear magnetization m_{NL}^x that is measured in experiment, as opposed to the individual susceptibilities [13]. The nonlinear magnetization contains contributions from $\chi^{(2)}$, $\chi^{(3;1)}$, and $\chi^{(3;2)}$, as well as higher order terms. The ratio of the intensities of these terms is, roughly speaking, determined by the strength of the THz field; n th order terms are proportional to the n th power of the THz field. Therefore, if there is a finite $\chi^{(2)}$, it will typically be the dominant contribution to the experimental

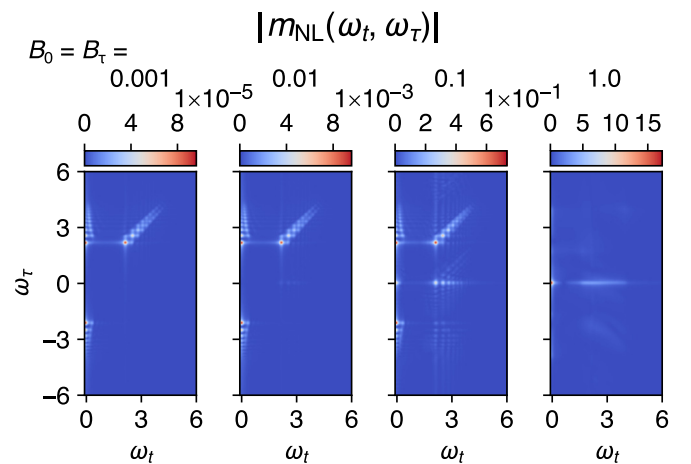


FIG. 10. Fourier transform of the nonlinear magnetization m_{NL} with increasing magnitude of incident THz pulses, B_0, B_τ , obtained by ED. The parameters for the weakly confined case, $J = 0.7$, $h_x = 0.3$, and $h_z = 0.06$ are used.

signal. Figure 10 shows the Fourier transform of the nonlinear magnetization m_{NL}^x obtained by ED with different strengths of the magnetic field pulses. The parameters for the weakly confined case, $J = 0.7$, $h_x = 0.3$, $h_z = 0.06$ are used. Up to $B_0 = B_\tau = 0.01$, the visible signal is dominated by the $\chi^{(2)}$ contribution. Only when $B_0 = B_\tau = 0.1$ is the visibility of the third-order contribution comparable to the second-order one, including the third-order pump-probe and rephasing signals. Finally, at $B_0 = B_\tau = 1.0$, the field pulses can no longer really be considered as perturbations, and the signal becomes dominated by the pump-probe response. To give an idea of the relative strength of the nonlinear signal, for $B_0 = B_\tau = 0.01$, the nonlinear magnetization, m_{NL}^x , is roughly 20 times smaller than the linear magnetization, m_0^x and m_τ^x . As a comparison, in the experiments of Ref. [13] on the canted antiferromagnet YFeO_3 , the measured m_{NL}^x is roughly 50 times smaller than the linear response.

Looking forward, there are a multitude of nonlinear many-body phenomena that can be further studied using ED and complementary analytical insights. For example, in ordered phases, the 2DCS signatures of nonlinear magnon decay and lifetime effects, or the interplay between distinct excitation modes. On the computational front, it would be useful to test the capabilities of ED in studying 2D spin models. As an example, there are already known analytical results for the nonlinear response of the Kitaev honeycomb model [27–29], which can be used to compare and contrast with ED results and to diagnose potential finite size effects. Taken together, it is clear that there is a wide world of exciting physics beyond the linear response regime still waiting to be explored.

The numerical data shown in the figures are available on Zenodo [48].

ACKNOWLEDGMENTS

We thank W. Choi, J. Knolle, and Y. Wan for illuminating discussions. We acknowledge partial funding from the DFG within Project-ID 277146847, SFB 1238 (projects C02,

C03). This work has benefited from multiple exchanges during the 2023 KITP workshop “A New Spin on Quantum Magnets,” supported in part by grant NSF PHY-1748958 to the Kavli Institute for Theoretical Physics (KITP). This work was performed, in part, in summer 2024 during the “Probing Collective Excitations in Quantum Matter by Transport and Spectroscopy” program at the Aspen Center for Physics, which is supported by National Science Foundation Grant No. PHY-2210452. The numerical simulations were performed on the JUWELS cluster at the Forschungszentrum Juelich and the Noctua2 cluster at PC2 in Paderborn.

APPENDIX A: FULL EXPRESSIONS FOR THE NONLINEAR SUSCEPTIBILITIES

For a multipulse setup of n delta-function pulses, as illustrated in Fig. 11, the time-dependent magnetic field can be written as

$$\mathbf{B}(t) = \mathbf{B}_0\delta(t) + \mathbf{B}_{t_1}\delta(t - t_1) + \dots + \mathbf{B}_{t_{n-1}}\delta(t - t_1 - \dots - t_{n-1}), \quad (\text{A1})$$

with t_m the delay time between the pulses at time $t_1 + \dots + t_{m-1}$ and at time $t_1 + \dots + t_m$, e.g., t_1 is the delay time between the pulses at times $t = t_0 = 0$ and $t = t_1$, and t_2 is the delay time between the pulses at times $t = t_1$ and $t = t_1 + t_2$. The general expression for the associated n th order susceptibility can be written as the equilibrium ground state expectation value of a nested commutator of $n + 1$ magnetization operators [32],

$$\begin{aligned} \chi_{\alpha\beta\gamma\dots\delta}^{(n)}(t_n, t_{n-1}, \dots, t_1) &= \frac{i^n}{2N} \langle [\dots [[M^\alpha(t_n + \dots + t_1), M^\beta(t_{n-1} + \dots + t_1)], \\ &\quad \times M^\gamma(t_{n-2} + \dots + t_1)], \dots], M^\delta(0) \rangle, \end{aligned} \quad (\text{A2})$$

where t_n is the time between the last pulse and the measurement of the α -component of the magnetization. The induced magnetization can then be expressed as

$$\begin{aligned} m^\alpha(t_n, \dots, t_1) &= \sum_{m=0}^{n-1} \sum_{\beta} \chi_{\alpha\beta}^{(1)}(t_{m+1} + \dots + t_n) B_{t_m}^\beta \\ &\quad + \frac{1}{2} \sum_{m=0}^{n-1} \sum_{l=0}^{n-1} \sum_{\beta, \gamma} \chi_{\alpha\beta\gamma}^{(2)}(t_{m+1} + \dots + t_n, t_{l+1} \\ &\quad + \dots + t_n) B_{t_m}^\beta B_{t_l}^\gamma + \dots \end{aligned} \quad (\text{A3})$$

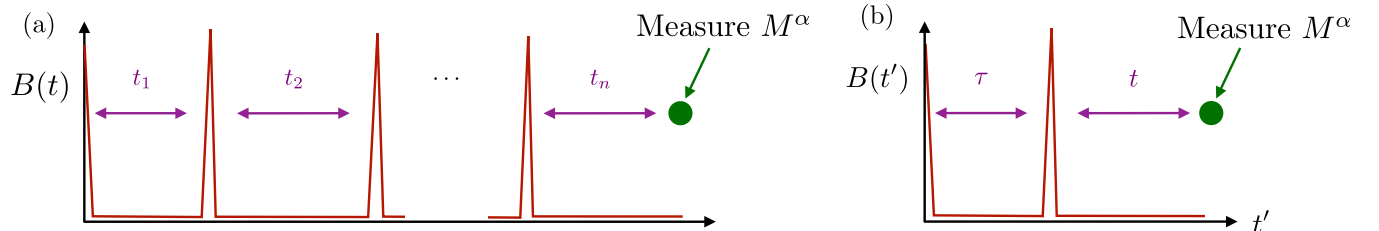


FIG. 11. The multipulse setup for the discussion in Appendix A is illustrated in (a), while the specific two-pulse setup used in the main text is shown again in (b).

1. First-order susceptibility

Assume that we have just a single delta-function magnetic field pulse at time $t = t_0 = 0$, so that the time-dependent magnetic field can be written as

$$\mathbf{B}(t) = \mathbf{B}_0\delta(t). \quad (\text{A4})$$

The first-order, or linear, magnetic susceptibility can be expressed as

$$\begin{aligned} \left(\frac{2N}{i}\right) \chi_{\alpha\beta}^{(1)}(t_1) &= \langle [M^\alpha(t_1), M^\beta(0)] \rangle \\ &= \langle M^\alpha(t_1)M^\beta(0) \rangle - \langle M^\beta(0)M^\alpha(t_1) \rangle \\ &= R_1^{\alpha\beta}(t_1) - [R_1^{\alpha\beta}(t_1)]^* \\ &= 2i\text{Im}[R_1^{\alpha\beta}(t_1)], \\ \Rightarrow \chi_{\alpha\beta}^{(1)}(t_1) &= -\frac{1}{N} \text{Im}[R_1^{\alpha\beta}(t_1)], \end{aligned} \quad (\text{A5})$$

where we have defined the function $R_1^{\alpha\beta}(t_1)$ as

$$R_1^{\alpha\beta}(t_1) = \langle M^\alpha(t_1)M^\beta(0) \rangle. \quad (\text{A6})$$

Note that in the definition of the time-dependent susceptibility, we have omitted a Heaviside θ -function, $\theta(t_1)$, which ensures causality of the response, and will instead include it only later when we define the Fourier transform.

Defining the matrix element $m_{fi}^\alpha = \langle f | M^\alpha | i \rangle = \sum_j \langle f | S_j^\alpha | i \rangle$, and fixing the energy such that $E_0 = 0$, meaning that all energies are measured relative to the ground state, we can insert resolutions of the identity and simplify R_1 as

$$\begin{aligned} R_1^{\alpha\beta}(t_1) &= \langle 0 | e^{iHt_1} M^\alpha e^{-iHt_1} M^\beta | 0 \rangle \\ &= \langle 0 | M^\alpha e^{-iHt_1} \sum_P | P \rangle \langle P | M^\beta | 0 \rangle \\ &= \sum_P \langle 0 | M^\alpha | P \rangle \langle P | M^\beta | 0 \rangle e^{-iE_P t_1} \\ &= \sum_P m_{0P}^\alpha m_{P0}^\beta e^{-iE_P t_1}. \end{aligned} \quad (\text{A7})$$

This allows us to write a simple expression for the first-order susceptibility in terms of matrix elements of the magnetization operator times an oscillating sine function,

$$\chi_{\alpha\beta}^{(1)}(t_1) = \frac{1}{N} \sum_P m_{0P}^\alpha m_{P0}^\beta \sin(E_P t_1). \quad (\text{A8})$$

Note that, in the above expression, we have explicitly assumed that the relevant product of matrix elements is real. Otherwise, there would be an additional cosine term times the imaginary part of the product. To simplify the remaining discussion, hereafter, we explicitly assume all relevant products of matrix elements are real.

Switching from time to frequency space, the Fourier transform of the susceptibility is

$$\chi_{\alpha\beta}^{(1)}(\omega_1) = \int dt_1 \theta(t_1) \chi_{\alpha\beta}^{(1)}(t_1) e^{-i\omega_1 t_1}. \quad (\text{A9})$$

Note that here we have now included the Heaviside θ -function to implement the positive time constraint $t_1 > 0$. In order to take the Fourier transform, we need to make use of the identity $\int dt \theta(t) e^{-i(\omega-E)t} = \pi \delta(\omega-E) - \mathcal{P} \frac{i}{\omega-E}$, with \mathcal{P} denoting the principal value (which, for simplicity, we omit in the following). The real part of the frequency-dependent susceptibility is then given by

$$\text{Re}[\chi_{\alpha\beta}^{(1)}(\omega_1)] = -\frac{1}{2N} \sum_P m_{0P}^\alpha m_{P0}^\beta \left[\frac{1}{\omega_1 - E_P} - \frac{1}{\omega_1 + E_P} \right], \quad (\text{A10})$$

while the imaginary part is given by

$$\text{Im}[\chi_{\alpha\beta}^{(1)}(\omega_1)] = -\frac{\pi}{2N} \sum_P m_{0P}^\alpha m_{P0}^\beta [\delta(\omega_1 - E_P) - \delta(\omega_1 + E_P)]. \quad (\text{A11})$$

The real and imaginary parts are often referred to as the reactive and absorptive (or dissipative) parts respectively. Crucially, the imaginary part isolates purely the matrix elements of interest, while the real part involves broadening in the form of $1/(\omega_1 \pm E_P)$.

In the special diagonal case of $\beta = \alpha$, we have an even more compact form of the susceptibility as

$$\chi_{\alpha\alpha}^{(1)}(t_1) = \frac{1}{N} \sum_P |m_{0P}^\alpha|^2 \sin(E_P t_1). \quad (\text{A12})$$

2. Second-order susceptibility

Assume now that we have two delta-function magnetic field pulses, at times $t = 0$ and $t = t_1$, so that the time-dependent magnetic field can be written as

$$\mathbf{B}(t) = \mathbf{B}_0 \delta(t) + \mathbf{B}_1 \delta(t - t_1). \quad (\text{A13})$$

The second-order *nonlinear* magnetic susceptibility can then be expressed as

$$\begin{aligned} \left(\frac{2N}{i^2}\right) \chi_{\alpha\beta\gamma}^{(2)}(t_2, t_1) &= \langle [[M^\alpha(t_2 + t_1), M^\beta(t_1)], M^\gamma(0)] \rangle \\ &= \langle M^\alpha(t_2 + t_1) M^\beta(t_1) M^\gamma(0) \rangle + \langle M^\gamma(0) M^\beta(t_1) M^\alpha(t_2 + t_1) \rangle \\ &\quad - \langle M^\beta(t_1) M^\alpha(t_2 + t_1) M^\gamma(0) \rangle - \langle M^\gamma(0) M^\alpha(t_2 + t_1) M^\beta(t_1) \rangle \\ &= R_1^{\alpha\beta\gamma}(t_2, t_1) + [R_1^{\alpha\beta\gamma}(t_2, t_1)]^* - [R_2^{\alpha\beta\gamma}(t_2, t_1) + [R_2^{\alpha\beta\gamma}(t_2, t_1)]^*] \\ &= 2\text{Re}[R_1^{\alpha\beta\gamma}(t_2, t_1) - R_2^{\alpha\beta\gamma}(t_2, t_1)], \\ \Rightarrow \chi_{\alpha\beta\gamma}^{(2)}(t_2, t_1) &= -\frac{1}{N} \text{Re}[R_1^{\alpha\beta\gamma}(t_2, t_1) - R_2^{\alpha\beta\gamma}(t_2, t_1)], \end{aligned} \quad (\text{A14})$$

where t_2 is the time between the second pulse, at time $t = t_1$, and the measurement of the α -component of the magnetization. The R_a functions in this case are defined as

$$R_1^{\alpha\beta\gamma}(t_2, t_1) = \langle M^\alpha(t_2 + t_1) M^\beta(t_1) M^\gamma(0) \rangle, \quad (\text{A15})$$

$$R_2^{\alpha\beta\gamma}(t_2, t_1) = \langle M^\beta(t_1) M^\alpha(t_2 + t_1) M^\gamma(0) \rangle. \quad (\text{A16})$$

Similar to the first-order case, we can, by inserting resolutions of the identity, alternatively write these as

$$R_1^{\alpha\beta\gamma}(t_2, t_1) = \sum_{PQ} m_{0Q}^\alpha m_{QP}^\beta m_{P0}^\gamma e^{-iE_P t_1} e^{-iE_Q t_2}, \quad (\text{A17})$$

$$R_2^{\alpha\beta\gamma}(t_2, t_1) = \sum_{PQ} m_{0Q}^\beta m_{QP}^\alpha m_{P0}^\gamma e^{-iE_P t_1} e^{-i(E_P - E_Q) t_2}. \quad (\text{A18})$$

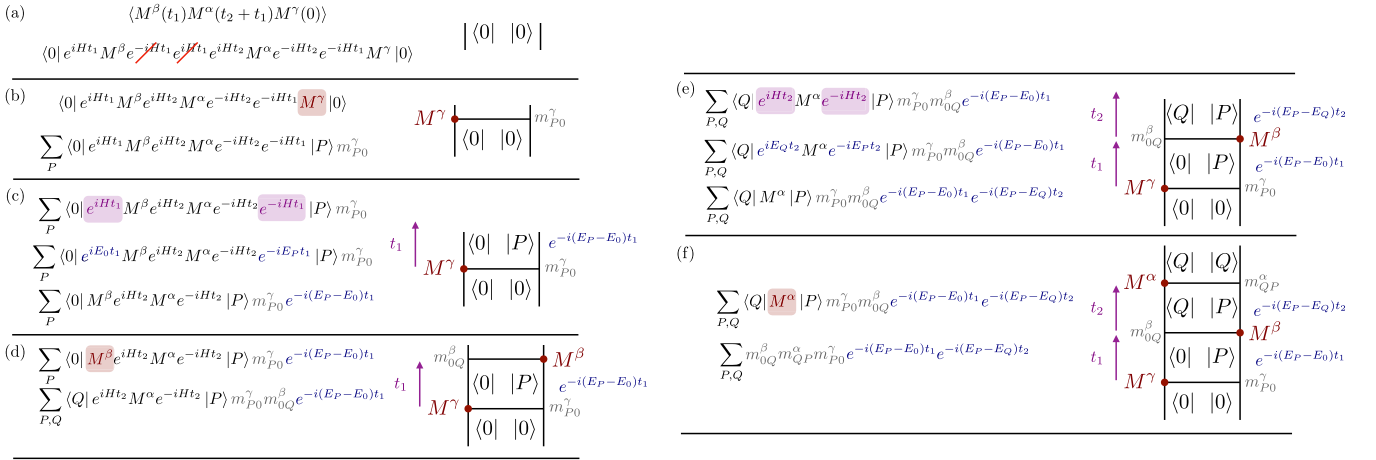


FIG. 12. Graphical representation of $R_2^{\alpha\beta\gamma}(t_2, t_1)$ for the second-order magnetic susceptibility. In (a)–(f), the individual steps in building up the final diagram are shown.

These R_a processes can be neatly summarized in graphical form using Liouville pathways and double-sided Feynman diagrams [32]. Such diagrams are commonly used in the field of nonlinear optics, and are based on a density-matrix description of the response. This allows for a compact visual representation that includes both emission and absorption, as well as keeping track of the wave vector of the pulses. In Fig. 12, we illustrate the individual steps in constructing a slightly alternate form of such a diagram, which focuses on the Heisenberg representation of the magnetization operators appearing in the dynamical correlation functions of interest for the magnetic susceptibilities. In Fig. 13, the resulting diagrams for both the first- and second-order susceptibility are shown. They are almost identical to the diagrams shown in Ref. [28] but with bras and kets reversed.

Now, defining the energy difference $\Delta E_{PQ} = E_P - E_Q$, the second-order susceptibility can be written (again, assuming the relevant matrix elements are real) in the time domain as

$$\chi_{\alpha\beta\gamma}^{(2)}(t_2, t_1) = -\frac{1}{N} \sum_{PQ} [m_{0Q}^\alpha m_{QP}^\beta m_{P0}^\gamma \cos(E_P t_1 + E_Q t_2) - m_{0Q}^\beta m_{QP}^\alpha m_{P0}^\gamma \cos(E_P t_1 + \Delta E_{PQ} t_2)]. \quad (\text{A19})$$

To convert to frequency space, we need to Fourier transform the above second-order susceptibility, taking into account the positive time constraints $t_2 > 0, t_1 > 0$,

$$\chi_{\alpha\beta\gamma}^{(2)}(\omega_2, \omega_1) = \int dt_2 \int dt_1 \theta(t_2) \theta(t_1) \chi_{\alpha\beta\gamma}^{(2)}(t_2, t_1) e^{-i\omega_2 t_2} e^{-i\omega_1 t_1}. \quad (\text{A20})$$

Again, making use of the fact that $\int dt \theta(t) e^{-i(\omega-E)t} = \pi \delta(\omega - E) - \mathcal{P} \frac{i}{\omega - E}$, we can separate out the real and imaginary parts of the frequency-dependent second-order susceptibility, with the real part given by

$$\begin{aligned} \text{Re}[\chi_{\alpha\beta\gamma}^{(2)}(\omega_2, \omega_1)] = & -\frac{1}{2N} \sum_{PQ} \left(m_{0Q}^\alpha m_{QP}^\beta m_{P0}^\gamma \left[\pi^2 \delta(\omega_1 - E_P) \delta(\omega_2 - E_Q) - \frac{1}{\omega_1 - E_P} \frac{1}{\omega_2 - E_Q} + (E \rightarrow -E) \right] \right. \\ & \left. - m_{0Q}^\beta m_{QP}^\alpha m_{P0}^\gamma \left[\pi^2 \delta(\omega_1 - E_P) \delta(\omega_2 - \Delta E_{PQ}) - \frac{1}{\omega_1 - E_P} \frac{1}{\omega_2 - \Delta E_{PQ}} + (E \rightarrow -E) \right] \right). \quad (\text{A21}) \end{aligned}$$

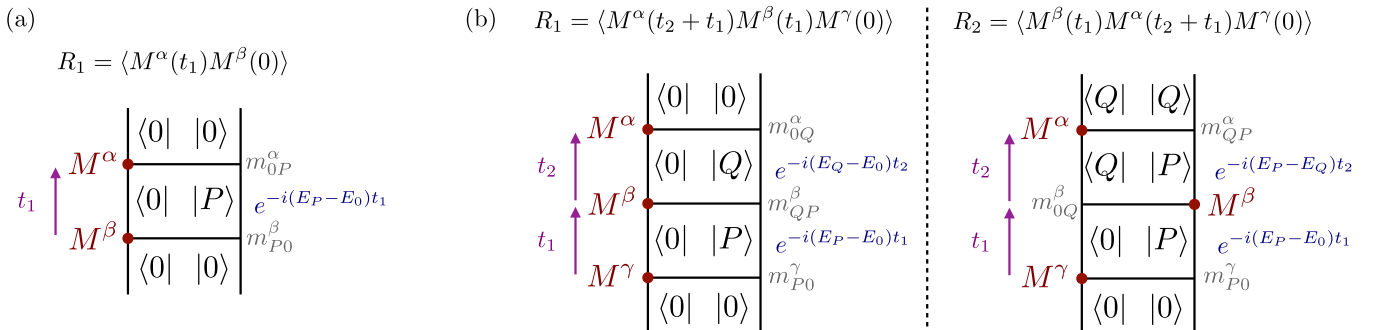


FIG. 13. Double-sided diagrams for the R_a processes contributing to (a) the linear susceptibility and (b) the second-order susceptibility.

and the imaginary part by

$$\begin{aligned} \text{Im}[\chi_{\alpha\beta\gamma}^{(2)}(\omega_2, \omega_1)] &= \frac{\pi}{2N} \sum_{PQ} \left(m_{0Q}^\alpha m_{QP}^\beta m_{P0}^\gamma \left[\frac{\delta(\omega_1 - E_P)}{\omega_2 - \Delta E_{PQ}} + \frac{\delta(\omega_2 - \Delta E_{PQ})}{\omega_1 - E_P} + (E \rightarrow -E) \right] \right. \\ &\quad \left. - m_{0Q}^\beta m_{QP}^\alpha m_{P0}^\gamma \left[\frac{\delta(\omega_1 - E_P)}{\omega_2 - \Delta E_{PQ}} + \frac{\delta(\omega_2 - \Delta E_{PQ})}{\omega_1 - E_P} + (E \rightarrow -E) \right] \right). \end{aligned} \quad (\text{A22})$$

Unlike the first-order case, here both the real and imaginary parts pick up unwanted broadening factors of the form $1/(\omega \pm E)$. This means that neither signal isolates the matrix element peaks themselves, contaminating any easy interpretation. As discussed in the main text, this situation, often referred to as ‘‘phase twisting’’ [16,25,26,33], arises due to the positive time constraint $t_2 > 0, t_1 > 0$ used in the Fourier transform. This can be more clearly observed by focusing on just the time-dependent parts of the calculation

$$\begin{aligned} \int dt_2 \int dt_1 \theta(t_2)\theta(t_1) e^{-i(\omega_2 - E_2)t_2} e^{-i(\omega_1 - E_1)t_1} &= \left(\pi \delta(\omega_1 - E_1) - \frac{i}{\omega_1 - E_1} \right) \left(\pi \delta(\omega_2 - E_2) - \frac{i}{\omega_2 - E_2} \right), \\ &= \left[\pi^2 \delta(\omega_1 - E_1) \delta(\omega_2 - E_2) - \frac{1}{\omega_1 - E_1} \frac{1}{\omega_2 - E_2} \right] \\ &\quad - i\pi \left[\frac{\delta(\omega_1 - E_1)}{\omega_2 - E_2} + \frac{\delta(\omega_2 - E_2)}{\omega_1 - E_1} \right], \end{aligned} \quad (\text{A23})$$

where we see that both real and imaginary parts include unwanted broadening factors. As discussed in the main text, and further in Appendix D, this issue can be avoided by relaxing the constraint to include strict positivity on only one of the time arguments, say t_2 . In that case, the resulting real part will only involve pure matrix element contributions

$$\begin{aligned} \text{Re}[\chi_{\alpha\beta\gamma}^{(2)}(\omega_2, \omega_1)] &= \text{Re} \left[\int dt_2 \int dt_1 \theta(t_2) \chi_{\alpha\beta\gamma}^{(2)}(t_2, t_1) e^{-i\omega_2 t_2} e^{-i\omega_1 t_1} \right] \\ &= -\frac{\pi}{N} \sum_{PQ} [m_{0Q}^\alpha m_{QP}^\beta m_{P0}^\gamma \delta(\omega_1 - E_P) \delta(\omega_2 - E_Q) - m_{0Q}^\beta m_{QP}^\alpha m_{P0}^\gamma \delta(\omega_1 - E_P) \delta(\omega_2 - \Delta E_{PQ}) + (E \rightarrow -E)]. \end{aligned} \quad (\text{A24})$$

Finally, we note again that, in the special case of $\gamma = \beta = \alpha$, the second-order susceptibility, in the time domain, can be simplified by taking out common matrix element factors as

$$\chi_{\alpha\alpha\alpha}^{(2)}(t_2, t_1) = -\frac{1}{N} \sum_{PQ} m_{0Q}^\alpha m_{QP}^\alpha m_{P0}^\alpha [\cos(E_P t_1 + E_Q t_2) - \cos(E_P t_1 + \Delta E_{PQ} t_2)]. \quad (\text{A25})$$

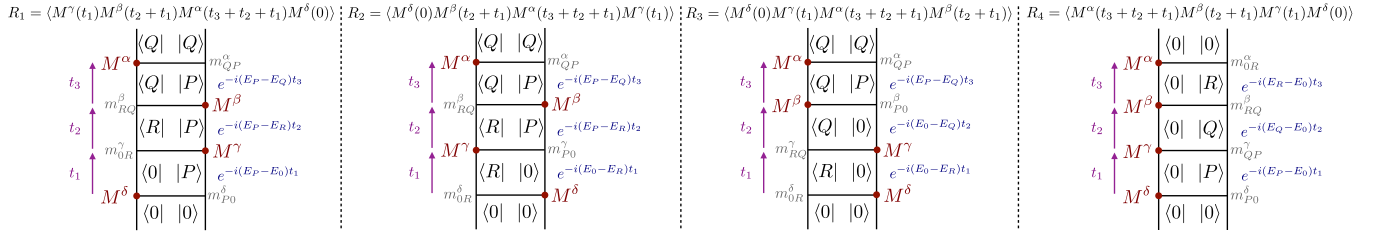
3. Third-order susceptibility

Assume now that we have three delta-function magnetic field pulses, at times $t = 0, t = t_1$ and $t = t_2$, so that the time-dependent magnetic field can now be written as

$$\mathbf{B}(t) = \mathbf{B}_0 \delta(t) + \mathbf{B}_{t_1} \delta(t - t_1) + \mathbf{B}_{t_2} \delta(t - t_1 - t_2). \quad (\text{A26})$$

The resulting third-order *nonlinear* magnetic susceptibility is

$$\begin{aligned} \left(\frac{2N}{i^3} \right) \chi_{\alpha\beta\gamma\delta}^{(3)}(t_3, t_2, t_1) &= \langle [[[M^\alpha(t_3 + t_2 + t_1), M^\beta(t_2 + t_1)], M^\gamma(t_1)], M^\delta(0)] \rangle \\ &= \langle M^\gamma(t_1) M^\beta(t_2 + t_1) M^\alpha(t_3 + t_2 + t_1) M^\delta(0) \rangle - \langle M^\delta(0) M^\alpha(t_3 + t_2 + t_1) M^\beta(t_2 + t_1) M^\gamma(t_1) \rangle \\ &\quad + \langle M^\delta(0) M^\beta(t_2 + t_1) M^\alpha(t_3 + t_2 + t_1) M^\gamma(t_1) \rangle - \langle M^\gamma(t_1) M^\alpha(t_3 + t_2 + t_1) M^\beta(t_2 + t_1) M^\delta(0) \rangle \\ &\quad + \langle M^\delta(0) M^\gamma(t_1) M^\alpha(t_3 + t_2 + t_1) M^\beta(t_2 + t_1) \rangle - \langle M^\beta(t_2 + t_1) M^\alpha(t_3 + t_2 + t_1) M^\gamma(t_1) M^\delta(0) \rangle \\ &\quad + \langle M^\alpha(t_3 + t_2 + t_1) M^\beta(t_2 + t_1) M^\gamma(t_1) M^\delta(0) \rangle - \langle M^\delta(0) M^\gamma(t_1) M^\beta(t_2 + t_1) M^\alpha(t_3 + t_2 + t_1) \rangle \\ &= R_1^{\alpha\beta\gamma\delta}(t_3, t_2, t_1) - [R_1^{\alpha\beta\gamma\delta}(t_3, t_2, t_1)]^* + R_2^{\alpha\beta\gamma\delta}(t_3, t_2, t_1) - [R_2^{\alpha\beta\gamma\delta}(t_3, t_2, t_1)]^* \\ &\quad + R_3^{\alpha\beta\gamma\delta}(t_3, t_2, t_1) - [R_3^{\alpha\beta\gamma\delta}(t_3, t_2, t_1)]^* + R_4^{\alpha\beta\gamma\delta}(t_3, t_2, t_1) - [R_4^{\alpha\beta\gamma\delta}(t_3, t_2, t_1)]^* \\ &= 2i \text{Im} [R_1^{\alpha\beta\gamma\delta}(t_3, t_2, t_1) + R_2^{\alpha\beta\gamma\delta}(t_3, t_2, t_1) + R_3^{\alpha\beta\gamma\delta}(t_3, t_2, t_1) + R_4^{\alpha\beta\gamma\delta}(t_3, t_2, t_1)], \\ \Rightarrow \chi_{\alpha\beta\gamma\delta}^{(3)}(t_3, t_2, t_1) &= \frac{1}{N} \text{Im} [R_1^{\alpha\beta\gamma\delta}(t_3, t_2, t_1) + R_2^{\alpha\beta\gamma\delta}(t_3, t_2, t_1) + R_3^{\alpha\beta\gamma\delta}(t_3, t_2, t_1) + R_4^{\alpha\beta\gamma\delta}(t_3, t_2, t_1)], \end{aligned} \quad (\text{A27})$$

FIG. 14. Double-sided diagrams for the four distinct R_a processes that contribute to the third-order susceptibility.

with t_3 the time between the second pulse, at $t = t_2 + t_1$, and the measurement of the α component of the magnetization. In this case, the R_a are defined as

$$R_1^{\alpha\beta\gamma\delta}(t_3, t_2, t_1) = \langle M^\gamma(t_1)M^\beta(t_2+t_1)M^\alpha(t_3+t_2+t_1)M^\delta(0) \rangle, \quad (\text{A28})$$

$$R_2^{\alpha\beta\gamma\delta}(t_3, t_2, t_1) = \langle M^\delta(0)M^\beta(t_2+t_1)M^\alpha(t_3+t_2+t_1)M^\gamma(t_1) \rangle, \quad (\text{A29})$$

$$R_3^{\alpha\beta\gamma\delta}(t_3, t_2, t_1) = \langle M^\delta(0)M^\gamma(t_1)M^\alpha(t_3+t_2+t_1)M^\beta(t_2+t_1) \rangle, \quad (\text{A30})$$

$$R_4^{\alpha\beta\gamma\delta}(t_3, t_2, t_1) = \langle M^\alpha(t_3+t_2+t_1)M^\beta(t_2+t_1)M^\gamma(t_1)M^\delta(0) \rangle. \quad (\text{A31})$$

Again, as before, we can express these in terms of magnetization matrix elements and time-dependent phase factors as

$$R_1^{\alpha\beta\gamma\delta}(t_3, t_2, t_1) = \sum_{PQR} m_{0R}^\gamma m_{RQ}^\beta m_{QP}^\alpha m_{P0}^\delta e^{-iE_{P0}t_1} e^{-i\Delta E_{PR}t_2} e^{-i\Delta E_{PQ}t_3}, \quad (\text{A32})$$

$$R_2^{\alpha\beta\gamma\delta}(t_3, t_2, t_1) = \sum_{PQR} m_{0R}^\delta m_{RQ}^\beta m_{QP}^\alpha m_{P0}^\gamma e^{+iE_{R0}t_1} e^{-i\Delta E_{PR}t_2} e^{-i\Delta E_{PQ}t_3}, \quad (\text{A33})$$

$$R_3^{\alpha\beta\gamma\delta}(t_3, t_2, t_1) = \sum_{PQR} m_{0R}^\delta m_{RQ}^\gamma m_{QP}^\alpha m_{P0}^\beta e^{+iE_{R0}t_1} e^{+iE_{Q0}t_2} e^{-i\Delta E_{PQ}t_3}, \quad (\text{A34})$$

$$R_4^{\alpha\beta\gamma\delta}(t_3, t_2, t_1) = \sum_{PQR} m_{0R}^\alpha m_{RQ}^\beta m_{QP}^\gamma m_{P0}^\delta e^{-iE_{P0}t_1} e^{-iE_{Q0}t_2} e^{-iE_{R0}t_3}. \quad (\text{A35})$$

The corresponding diagrams for these four R_a processes are shown in Fig. 14. This allows us to rewrite the susceptibility in the time domain as

$$\begin{aligned}
\chi_{\alpha\beta\gamma\delta}^{(3)}(t_3, t_2, t_1) = & -\frac{1}{N} \sum_{PQR} [m_{0R}^\gamma m_{RQ}^\beta m_{QP}^\alpha m_{P0}^\delta \sin(E_{P0}t_1 + \Delta E_{PR}t_2 + \Delta E_{PQ}t_3) \\
& + m_{0R}^\delta m_{RQ}^\beta m_{QP}^\alpha m_{P0}^\gamma \sin(-E_{R0}t_1 + \Delta E_{PR}t_2 + \Delta E_{PQ}t_3) + m_{0R}^\delta m_{RQ}^\gamma m_{QP}^\alpha m_{P0}^\beta \sin(-E_{R0}t_1 - E_{Q0}t_2 + \Delta E_{PQ}t_3) \\
& + m_{0R}^\alpha m_{RQ}^\beta m_{QP}^\gamma m_{P0}^\delta \sin(E_{P0}t_1 + E_{Q0}t_2 + E_{R0}t_3)]. \quad (\text{A36})
\end{aligned}$$

Again, in the general case in which the relevant products of matrix elements above have both real and imaginary parts, there would also be cosine factors present proportional to the imaginary parts of the products. Note that, for $|Q\rangle = |0\rangle$, the matrix elements reduce to a product of linear response matrix elements, e.g., in the first term, we would get $[m_{0R}^\gamma m_{R0}^\beta][m_{0P}^\alpha m_{P0}^\delta]$, which are precisely the matrix elements that appear in $\chi_{\gamma\beta}^{(1)}$ and $\chi_{\alpha\delta}^{(1)}$. The case $|Q\rangle = |0\rangle$ thus contains similar information as the linear response (it is in a sense ‘‘linear response squared’’). Switching to the frequency domain now involves a three-dimensional Fourier transform over t_1 , t_2 , and t_3 ,

$$\chi_{\alpha\beta\gamma\delta}^{(3)}(\omega_3, \omega_2, \omega_1) = \int dt_3 \int dt_2 \int dt_1 \theta(t_3)\theta(t_2)\theta(t_1)\chi_{\alpha\beta\gamma\delta}^{(3)}(t_3, t_2, t_1) e^{-i\omega_3 t_3} e^{-i\omega_2 t_2} e^{-i\omega_1 t_1}. \quad (\text{A37})$$

We will not write the full expressions here for the real and imaginary parts of $\chi_{\alpha\beta\gamma\delta}^{(3)}(\omega_3, \omega_2, \omega_1)$. However, their structure can be straightforwardly gleaned from the discussion of the second-order susceptibility. For the third-order case, the real part will involve contributions of the form $[\delta(\omega_1 - E_1)\delta(\omega_2 - E_2)]/(\omega_3 - E_3)$ and $1/[(\omega_1 - E_1)(\omega_2 - E_2)(\omega_3 - E_3)]$, while the imaginary part will involve contributions of the form $\delta(\omega_1 - E_1)\delta(\omega_2 - E_2)\delta(\omega_3 - E_3)$ and $\delta(\omega_1 - E_1)/[(\omega_2 - E_2)(\omega_3 - E_3)]$. Once again, as expected for the nonlinear susceptibilities, both parts are contaminated by broadening factors. In order to eliminate such broadening, the positive time constraint needs again to be relaxed, to include strict positivity for only one of the three time arguments. This is illustrated explicitly in Appendix D for the two-pulse case, with the clean broadening-free signal shown in Fig. 16.

In the case of 2DCS, only two pulses are used and so this results in two distinct third-order susceptibilities, defined as $\chi^{(3;1)}$ for $t_1 = 0$ and $\chi^{(3;2)}$ for $t_2 = 0$. This results in the following relationships between the associated R_a processes:

$$\chi_{\alpha\beta\gamma\gamma}^{(3;1)}(t_3, t_2, 0) : R_1^{\alpha\beta\gamma\gamma}(t_3, t_2, 0) = R_2^{\alpha\beta\gamma\gamma}(t_3, t_2, 0), \quad (\text{A38})$$

$$\chi_{\alpha\beta\beta\delta}^{(3;2)}(t_3, 0, t_1) : R_2^{\alpha\beta\beta\delta}(t_3, 0, t_1) = R_3^{\alpha\beta\beta\delta}(t_3, 0, t_1). \quad (\text{A39})$$

In the special case of a diagonal susceptibility $\chi_{\alpha\alpha\alpha\alpha}^{(3;1,2)}$ as, for example, studied in the main text, we have simply $R_1 = R_2$ for the $\chi^{(3;1)}$ case, and $R_2 = R_3$ for the $\chi^{(3;2)}$ case.

Using τ and t as the time delay between the two pulses and the measurement time respectively, this leads to the following expression for $\chi^{(3;1)}$ in the time domain:

$$\begin{aligned} \chi_{\alpha\beta\gamma\delta}^{(3;1)}(t, \tau, 0) = & -\frac{1}{N} \sum_{PQR} [m_{0R}^\gamma m_{RQ}^\beta m_{QP}^\alpha m_{P0}^\delta \sin(\Delta E_{PR}\tau + \Delta E_{PQ}t) + m_{0R}^\delta m_{RQ}^\beta m_{QP}^\alpha m_{P0}^\gamma \sin(\Delta E_{PR}\tau + \Delta E_{PQ}t) \\ & + m_{0R}^\delta m_{RQ}^\gamma m_{QP}^\alpha m_{P0}^\beta \sin(-E_Q\tau + \Delta E_{PQ}t) + m_{0R}^\alpha m_{RQ}^\beta m_{QP}^\gamma m_{P0}^\delta \sin(E_Q\tau + E_Rt)]. \end{aligned}$$

For $|Q\rangle = |0\rangle$, and thus $E_Q = 0$, the final two terms in $\chi^{(3;1)}$ take the form of PP signals. This is also the case for the first two terms if, in addition, $|P\rangle = |R\rangle$. On the other hand, $\chi^{(3;2)}$ in the time domain is written as

$$\begin{aligned} \chi_{\alpha\beta\gamma\delta}^{(3;2)}(t, 0, \tau) = & -\frac{1}{N} \sum_{PQR} [m_{0R}^\gamma m_{RQ}^\beta m_{QP}^\alpha m_{P0}^\delta \sin(E_P\tau + \Delta E_{PQ}t) + m_{0R}^\delta m_{RQ}^\beta m_{QP}^\alpha m_{P0}^\gamma \sin(-E_R\tau + \Delta E_{PQ}t) \\ & + m_{0R}^\delta m_{RQ}^\gamma m_{QP}^\alpha m_{P0}^\beta \sin(-E_R\tau + \Delta E_{PQ}t) + m_{0R}^\alpha m_{RQ}^\beta m_{QP}^\gamma m_{P0}^\delta \sin(E_P\tau + E_Rt)]. \end{aligned}$$

For $|Q\rangle = |0\rangle$, and thus $E_Q = 0$, the first term in $\chi^{(3;2)}$ will take the form of a diagonal NR signal. In addition, the final term takes the form of diagonal ($P = R$) and off-diagonal ($P \neq R$) NR signals, and the second and third terms diagonal ($P = R$) and off-diagonal ($P \neq R$) R signals. It should be noted that whether such signals are observed in the final susceptibility of course depends on the corresponding matrix elements being finite and the different terms in the sum over intermediate states combining constructively (as, in many cases, cancellations can occur which suppress certain signals). In any case, the above $|Q\rangle = |0\rangle$ considerations illustrate that it is rather natural to observe PP signals in $\chi^{(3;1)}$ and NR and R signals in $\chi^{(3;2)}$.

4. n th-order susceptibility

At n th order, the general expression for the susceptibility in the time domain is

$$\begin{aligned} \chi_{\alpha\beta\gamma\dots\delta}^{(n)}(t_n, t_{n-1}, \dots, t_1) &= \frac{i^n}{2N} \langle [\dots [M^\alpha(t_n + \dots + t_1), M^\beta(t_{n-1} + \dots + t_1)], \\ &\quad \times M^\gamma(t_{n-2} + \dots + t_1), \dots], M^\delta(0) \rangle. \end{aligned} \quad (\text{A40})$$

Thus, at n th order, there will be 2^n terms total, giving 2^{n-1} unique R_a contributions. For n even, $\chi^{(n)}$ will be written as the real part of the sum of R_a processes, $\chi^{(n)} \propto \text{Re}[R_1 + \dots + R_{2^{n-1}}]$, and in frequency space the real part will be of central interest if both positive and negative time arguments are considered. On the other hand, for n odd, $\chi^{(n)} \propto \text{Im}[R_1 + \dots + R_{2^{n-1}}]$, and in frequency space the imaginary part will be of central interest if both positive and negative time arguments are considered.

APPENDIX B: PREPARATION OF THE THERMAL STATE

The thermal state $|\phi\rangle$, which is used to calculate specific heat and 2DCS, is obtained by the imaginary time evolution of

the initial state $|\phi_0\rangle$. Instead of computing $|\phi\rangle$ directly, we first compute $e^{\beta(l-H)/2} |\phi_0\rangle$, where l is set to larger than the largest eigenvalue of H . The expansion of the exponential operator is given by

$$e^{\beta(l-H)/2} |\phi_0\rangle = \sum_{k=0}^{\infty} \frac{(\beta/2)^k}{k!} (l-H)^k |\phi_0\rangle = \sum_{k=0}^{\infty} \frac{(\beta/2)^k}{k!} |k\rangle, \quad (\text{B1})$$

It is known that the relevant terms in the sum is localized in the range $|k^* - k| = o(L)$, where the temperature of normalized microcanonical thermal pure quantum state $|\phi_{k^*}\rangle = |k^*\rangle / \| |k^*\rangle \|$ is close to $1/\beta$ [35,36]. We choose the number of iterations as $k_{\max} = 2000$, which is sufficiently large for the temperature range we are interested in in this study. Then, multiplying scalar $e^{-\beta l/2}$ to this state gives $|\phi\rangle$. Similarly to the linear response [49], we calculate the nonlinear susceptibility from the time evolution of $|\phi\rangle$.

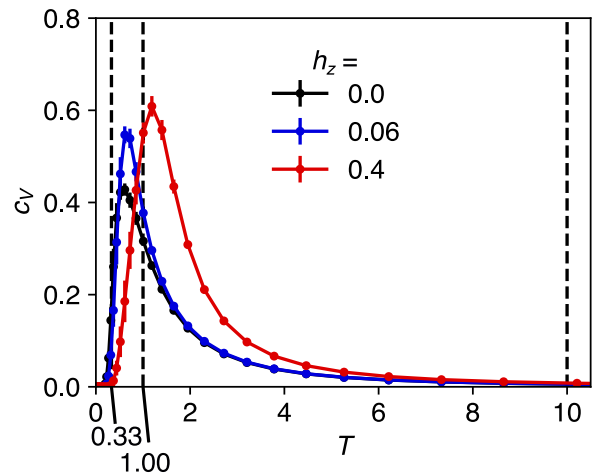


FIG. 15. Specific heat c_V of 1D-TFIM in the longitudinal field from ED with $L = 16$. The parameters $J = 0.7$, $h_x = 0.3$, and several values of h_z are considered.

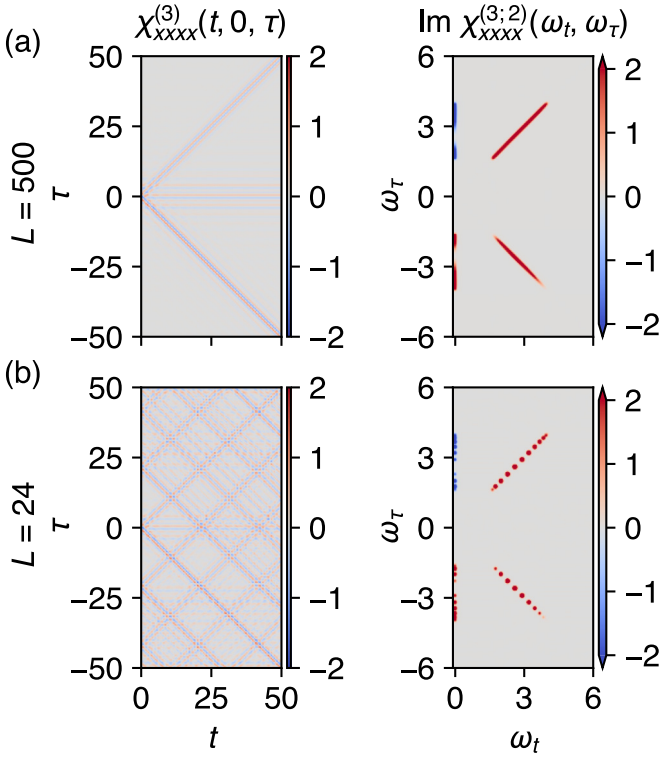


FIG. 16. Phase untwisted 2DCS obtained by including negative τ in the calculation. The parameters $J = 0.7$, $h_x = 0.3$, $h_z = 0.06$, and the system size $L = 500$ (a) and 24 (b) are used.

Figure 15 shows the calculated specific heat c_V with different values of h_z . The temperatures used for the finite temperature 2DCS are chosen to cover the different temperature regimes separated by the peaks of c_V .

APPENDIX C: ZERO/FINITE TEMPERATURE 2DCS IN TFIM

Here, we provide a 2DCS in TFIM based on Ref. [19]. With the Jordan-Wigner transformation,

$$\begin{aligned} \sigma_i^x &= 2c_i^\dagger c_i - 1, \\ \sigma_i^z &= (c_i^\dagger + c_i) \exp\left(i\pi \sum_{j=1}^{i-1} c_j^\dagger c_j\right), \end{aligned} \quad (\text{C1})$$

the Hamiltonian reads

$$\begin{aligned} \mathcal{H}_p &= -J \sum_{i=1}^{L-1} (c_i^\dagger - c_i)(c_{i+1}^\dagger + c_{i+1}) \\ &+ (-1)^p J (c_L^\dagger - c_L)(c_1^\dagger + c_1) - h_x \sum_{i=1}^L (2n_i - 1), \end{aligned} \quad (\text{C2})$$

where p is the parity of the number of fermions. Among 2^L Fock states of each fermionic Hamiltonian, only 2^{L-1} states with the same parity as p are correct states of the spin Hamiltonian with the periodic boundary condition. The ground state is known to lie in the parity even sector, therefore the contribution from parity odd sector becomes finite only at the finite

temperature 2DCS. We introduce the momentum representation of the fermionic operators as $c_j = (1/\sqrt{L}) \sum_k e^{ikj} c_k$, where $k = \pm(2n-1)\pi/L$ with $n = 1, \dots, L/2$ for parity even sector, and k satisfies $k = 2\pi n/L$ with $n = -L/2 + 1, \dots, 0, \dots, L/2$ for parity odd sector. Next, we introduce a pair Hamiltonian with momentums k and $-k$ as

$$\mathcal{H}_k = (c_k^\dagger, c_{-k}) \begin{pmatrix} \epsilon_k & i\Delta_k \\ -i\Delta_k & -\epsilon_k \end{pmatrix} \begin{pmatrix} c_k \\ c_{-k}^\dagger \end{pmatrix}, \quad (\text{C3})$$

where $\epsilon_k = -2J \cos k - 2h_x$ and $\Delta_k = -2J \sin k$, and a Hamiltonian for $k = 0$ and $k = \pi$ of the parity odd sector as

$$\mathcal{H}_{k=0, \pi} = -2J(n_0 - n_\pi) - 2h_x(n_0 + n_\pi - 1). \quad (\text{C4})$$

Now, we can rewrite the Hamiltonian of the even sector as

$$\mathcal{H}_0 = \sum_{k>0} \mathcal{H}_k \quad (\text{C5})$$

and the Hamiltonian of the odd sector as

$$\mathcal{H}_1 = \sum_{0 < k < \pi} \mathcal{H}_k + \mathcal{H}_{k=0, \pi}. \quad (\text{C6})$$

Performing the Bogoliubov transformation:

$$\begin{pmatrix} c_k \\ c_{-k}^\dagger \end{pmatrix} = \begin{pmatrix} \cos \frac{\theta_k}{2} & -i \sin \frac{\theta_k}{2} \\ -i \sin \frac{\theta_k}{2} & \cos \frac{\theta_k}{2} \end{pmatrix} \begin{pmatrix} \gamma_k \\ \gamma_{-k}^\dagger \end{pmatrix}, \quad (\text{C7})$$

where $\tan \theta_k = \Delta_k / \epsilon_k$, we obtain the diagonalized Hamiltonian

$$\mathcal{H}_k = \lambda_k (\gamma_k^\dagger \gamma_k - \gamma_{-k} \gamma_{-k}^\dagger), \quad (\text{C8})$$

where $\lambda_k = \sqrt{\epsilon_k^2 + \Delta_k^2}$.

Using the Anderson pseudospins:

$$\begin{aligned} \tau_k^x &= \gamma_{-k} \gamma_k + \gamma_k^\dagger \gamma_{-k}^\dagger, \\ \tau_k^y &= i(\gamma_{-k} \gamma_k - \gamma_k^\dagger \gamma_{-k}^\dagger), \\ \tau_k^z &= \gamma_k^\dagger \gamma_k - \gamma_{-k} \gamma_{-k}^\dagger, \end{aligned} \quad (\text{C9})$$

magnetization M^x is given by

$$\begin{aligned} M^x &= \frac{1}{2} \sum_{i=1}^L \sigma_i^x \\ &= \sum_{0 < k < \pi} (\cos \theta_k \tau_k^z + \sin \theta_k \tau_k^y), \\ &\equiv \sum_{0 < k < \pi} m_k^x, \end{aligned} \quad (\text{C10})$$

Note that we drop the contribution from $k = 0$ and $k = \pi$ in the odd sector, which is a constant of the motion and does not contribute to the 2DCS. In the Heisenberg picture, m_k^x becomes

$$m_k^x(t) = \cos \theta_k \tau_k^z + \sin \theta_k (\tau_k^y \cos(2\lambda_k t) + \tau_k^x \sin(2\lambda_k t)). \quad (\text{C11})$$

Using the fact that each m_k^x commutes with each other, the third-order response is given by

$$\begin{aligned}\chi_{xxxx}^{(3)}(t_3, t_2, t_1) &= \frac{1}{L} \sum_{0 < k < \pi} \langle [[[m_k^x(t_3 + t_2 + t_1), m_k^x(t_2 + t_1)], \\ &\quad \times m_k^x(t_1)], m_k^x(0)] \rangle \\ &= \frac{1}{L} \sum_{0 < k < \pi} [A_k^{(1)} + A_k^{(2)} + A_k^{(3)} + A_k^{(4)}],\end{aligned}\quad (\text{C12})$$

where

$$\begin{aligned}A_k^{(1)} &= 8 \sin^2 \theta_k \cos^2 \theta_k \sin(2\lambda_k(t_3 + t_2 + t_1)) \langle \tau_k^z \rangle, \\ A_k^{(2)} &= -8 \sin^2 \theta_k \cos^2 \theta_k \sin(2\lambda_k(t_2 + t_1)) \langle \tau_k^z \rangle, \\ A_k^{(3)} &= 4 \sin^4 \theta_k \sin(2\lambda_k(t_3 + t_1)) \langle \tau_k^z \rangle, \\ A_k^{(4)} &= 4 \sin^4 \theta_k \sin(2\lambda_k(t_3 - t_1)) \langle \tau_k^z \rangle,\end{aligned}\quad (\text{C13})$$

Here we utilized the fact that $\langle \tau_k^x \rangle = \langle \tau_k^y \rangle = 0$. Zero temperature limit Eq. (12) is obtained by $\langle \tau_k^z \rangle = -1$, and consider the even sector only, i.e., we take a sum for $k = (2n - 1)\pi/L$ with $n = 1, \dots, L/2$.

Finite temperature 2DCS is obtained by taking the thermal average of $\langle \tau_k^z \rangle$. The distribution function is given by

$$Z = \text{Tr}(e^{-\beta \mathcal{H}_{\text{spin}}}) = \sum_p \text{Tr}(P_p e^{-\beta \mathcal{H}_p}) \equiv \sum_p Z_p, \quad (\text{C14})$$

where P_p is the projection operator to the parity p sector defined as

$$P_p = \frac{1}{2} (1 + (-1)^p e^{-i\pi N}). \quad (\text{C15})$$

Z_0 can be computed as

$$Z_0 = \frac{e^{-\beta E_0}}{2} \left[\prod_k (1 + e^{-\beta \lambda_k}) + \prod_k (1 - e^{-\beta \lambda_k}) \right], \quad (\text{C16})$$

where $E_0 = -\sum_{k>0} \lambda_k$ is the ground state energy of the parity even sector, and the product over k runs the entire Brillouin zone. Similarly, Z_1 can be computed as

$$Z_1 = \frac{e^{-\beta E_1}}{2} \left[\prod_k (1 + e^{-\beta \lambda_k}) - \prod_k (1 - e^{-\beta \lambda_k}) \right], \quad (\text{C17})$$

where $E_1 = -\sum_{0 < k < \pi} \lambda_k + 2h_x$ is the energy of the state obtained by annihilating the $k = 0$ fermion from the odd-sector ground state. For $k = 0$ and π , we take $\lambda_0 = -2J - 2h_x$ and $\lambda_\pi = 2J - 2h_x$, respectively. Finally, we obtain

$$\langle \tau_k^z \rangle = -\frac{Z_{p,\bar{k}}(1 - e^{-2\beta \lambda_k})}{Z_0 + Z_1}, \quad (\text{C18})$$

where p is the parity that is consistent with k , and $Z_{p,\bar{k}}$ is obtained by omitting the contribution from $\pm k$ in the product over k .

APPENDIX D: PHASE UNTWISTED 2DCS

In the main text, we discussed how the positive time constraint leads to a distorted signal known as phase twisting, which can even eliminate the NR signal at $\omega_t = \omega_\tau$. We demonstrate that this issue can be resolved by incorporating

negative τ values, which is feasible in analytical calculations and ED simulations. Figure 16 presents the 2DCS results obtained by including negative τ . It is noteworthy that even for a substantially large system size ($L = 500$), the NR signal is observable. Furthermore, the data for $L = 24$ now appears as a discretized version of the $L = 500$ data. It is important to note that NR and R signals are not symmetric, as predicted by Eq. (12). Therefore phase untwisting cannot be simply achieved by symmetrizing the experimental data around about ω_τ [25].

APPENDIX E: FOUR-KINK APPROXIMATION

Here, we provide the detailed calculation of 2DCS using four-kink approximation. First, we consider the two-kink approximation. Two-kink model can be solved analytically, and it is sufficient to describe the linear response and the second-order response [22,37,44]. Next we discuss the necessity of the four-kink space to properly calculate third-order response, and then introduce the four-kink approximation.

As a first step, we approximate the ground state of the TFIM as a fully polarized FM state, $|0\rangle = |\uparrow\uparrow \dots \uparrow\rangle$. Then two-kink states can be expressed using two quantum numbers j and l , where j is the position of the first kink and l is the distance between the two kinks, i.e., $|j, l\rangle \equiv |\dots \uparrow\uparrow \downarrow_j \dots \downarrow_{(j+l-1)} \uparrow\uparrow \dots\rangle$. The projection to the subspace spanned by $|j, l\rangle$ gives TK Hamiltonian which acts as:

$$\begin{aligned}\mathcal{H}_{\text{TK}} |j, l\rangle &= (4J + 2lh_z) |j, l\rangle - h_x (|j, l+1\rangle + |j, l-1\rangle \\ &\quad + |j+1, l-1\rangle + |j-1, l+1\rangle),\end{aligned}\quad (\text{E1})$$

here we carefully omit the coupling between the two-kink sector and the ground state, i.e., the number of kinks is conserved. Kink number conservation can be justified for short times, as long as the system is in the deep inside the FM phase [45,46]. The coupling with the two-kink sector and the ground state is given by the external pulse field M^x acting as

$$M^x |0\rangle = \frac{1}{2} \sum_j |j, 1\rangle. \quad (\text{E2})$$

Then, using \mathcal{H}_{TK} for the time evolution, we can calculate 2DCS following the same procedure as described in the main text.

Comparing the results from the two-kink approximation and ED (Fig. 17), while they agree on most of the key qualitative features, there are significant quantitative differences. The two-kink approximation tends to overestimate the intensities compared to the ED data. This is particularly evident in the R and NR signals in $\chi_{xxxx}^{(3;2)}$. As discussed in the main text, this discrepancy arises because the two-kink approximation fails to fully account for the pole cancellations, which occur between the processes where the intermediate state $|Q\rangle$ is a four-kink state and the ground state.

Next, we introduce the four-kink basis $|j_1, l_1, j_2, l_2\rangle = |\uparrow\uparrow \downarrow_{j_1} \dots \downarrow_{(j_1+l_1-1)} \uparrow\uparrow \downarrow_{j_2} \dots \downarrow_{(j_2+l_2-1)} \uparrow\uparrow \dots\rangle$. The action

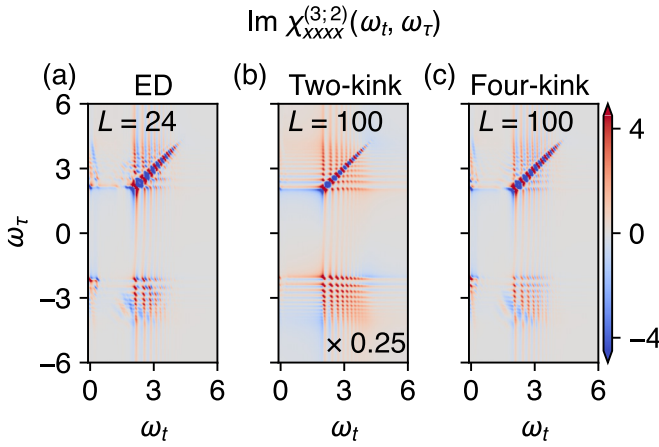


FIG. 17. 2DCS in the four-kink approximation for the TFIM obtained by (a) ED, (b) two-kink approximation, and (c) four-kink approximation. The parameters $J = 0.7$, $h_x = 0.3$, and $h_z = 0.06$ are used. For two-kink approximation, the results are scaled by a factor of 0.25 for better visualization.

of the four-kink Hamiltonian is given by

$$\begin{aligned} \mathcal{H}_{\text{FK}} |j_1, l_1, j_2, l_2\rangle &= [8J + 2(l_1 + l_2)h_z] |j_1, l_1, j_2, l_2\rangle \\ &\quad - h_x(|j_1, l_1 + 1, j_2, l_2\rangle + |j_1, l_1 - 1, j_2, l_2\rangle) \end{aligned}$$

$$\begin{aligned} &+ |j_1 + 1, l_1 - 1, j_2, l_2\rangle + |j_1 - 1, l_1 + 1, j_2, l_2\rangle \\ &+ |j_1, l_1, j_2, l_2 + 1\rangle + |j_1, l_1, j_2, l_2 - 1\rangle \\ &+ |j_1, l_1, j_2 + 1, l_2 - 1\rangle + |j_1, l_1, j_2 - 1, l_2 + 1\rangle). \end{aligned} \quad (\text{E3})$$

Again, we omit the coupling between the four-kink sector and the two-kink sector.

There are two possible ways to create a four-kink state from a two-kink state using the external pulse field M^x : either by creating another pair of kinks at a different position or by splitting the existing domain into two. Therefore the action of M^x on two-kink states is given by

$$\begin{aligned} M^x |j, l\rangle &= \frac{1}{2} \sum_{j'} |j, l, j', 1\rangle \\ &+ \frac{1}{2} \sum_{j'} |j, j' - j, j' + 1, l - j' + j - 1\rangle, \\ &+ (\text{two-kink states}) \\ &+ (\text{ground state}), \end{aligned} \quad (\text{E4})$$

where j' should be properly chosen to ensure the resulting state is a four-kink state. Note that, in addition to the transition to the four-kink sector, M^x acting on a two-kink state can also result in a transition to either the two-kink sector or the ground state, depending on the length of the domain.

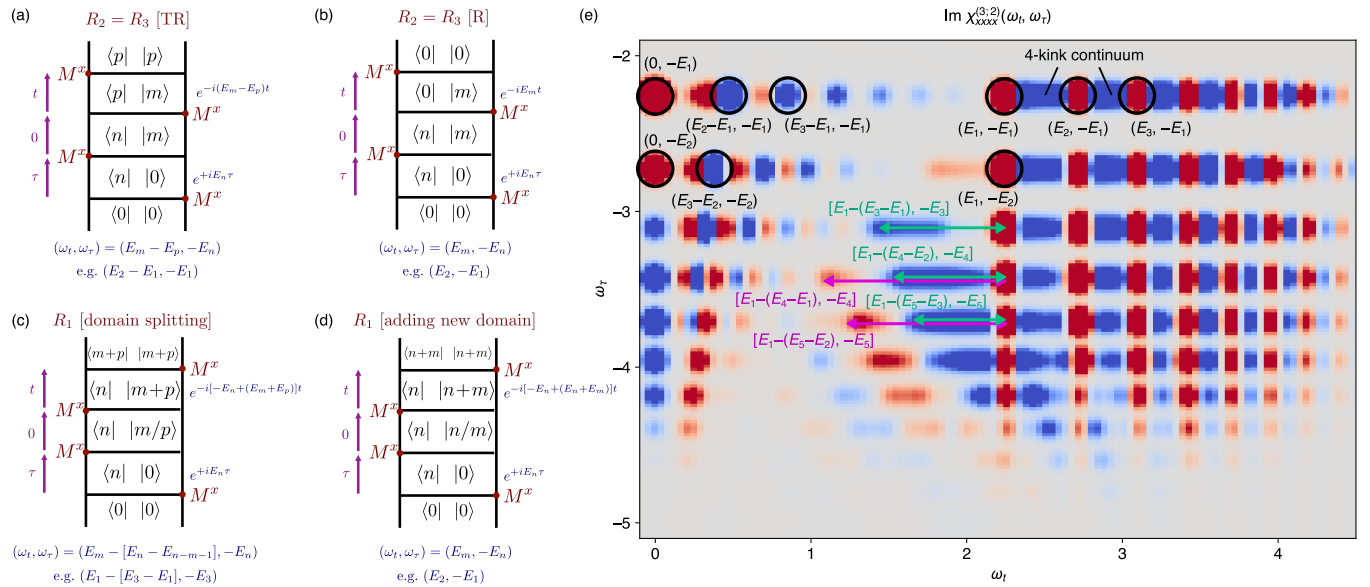


FIG. 18. Structure of $\chi_{xxxx}^{(3;2)}$ in lower quadrant. [(a)–(d)] Relevant double-sided Feynman diagrams. Below each diagram, the resulting signal location is indicated. (a) Terahertz rectification (TR) peaks originate from $R_2 = R_3$ processes, in which all intermediate states are two-kink states. The grid of peaks at $(E_m, -E_n)$ results from processes where the intermediate state $|Q\rangle$ is either the ground state (b) or a four-kink state (d). In (c), the intermediate four-kink state is created by splitting the existing domain, whereas in (d), the intermediate four-kink state is created by adding a new domain at a different location. Note that for the four-kink states, both spinon bound pairs carry equal and opposite momentum, forming a continuum of excitations. For simplicity, in all diagrams above, only the lowest energy state in which both spinon-bound pairs have zero momentum is shown. (e) The fourth quadrant of $\chi_{xxxx}^{(3;2)}$ obtained from the four-kink calculation. The data are phase-untwisted for better visualization. The parameters $J = 0.7$, $h_x = 0.3$, and $h_z = 0.1$ are used. The contributions from (b) and (d) partially cancel each other out, leaving the remaining signal visible at $(E_m, -E_n)$. The contribution from (c) is visible at $(E_1 - [E_n - E_{n-2}], -E_n)$. As an example, the contribution from the domain splitting process with single/two spin flips is indicated by green/pink colors. See Appendix E for a more detailed discussion. A selection of the TR peaks, originating from the process shown in (a), are also highlighted.

Once the decoupled two/four-kink Hamiltonian is constructed, we can again calculate the 2DCS using the same procedure as in the main text. As shown in Fig. 17, the four-kink approximation provides qualitatively better agreement with the ED data than the two-kink approximation. Specifically, there are no extensive poles remaining in the four-kink approximation, since the cancellation of poles between processes with an intermediate ground state and intermediate four-kink state is taken care of.

Note that by utilizing the translational invariance of the Hamiltonian, we can reduce the relevant quantum numbers from four to three. Therefore the dimension of the Hilbert space grows as $O(L^3)$, which is still manageable for system sizes up to $L \sim O(100)$.

APPENDIX F: DOMAIN SPLITTING PROCESSES AND TERAHERTZ RECTIFICATION SIGNALS

Here we complement the discussion in the main text of the rephasing signals by looking at the full set of signals in the $\omega_t > 0, \omega_\tau < 0$ quadrant. In particular, the phase untwisted version of the signals, presented in Fig. 18, provides a much cleaner and more insightful viewpoint on the structure of the 2DCS signal.

The terahertz rectification signal originates purely from two-kink processes, as illustrated in Fig. 18(a). The first pulse creates a bound state with energy E_n , and the second pulse changes this to a bound state with energy E_p , while also creating a bound state with energy E_m with the opposite frequency. This $R_2 = R_3$ process generates peaks at $(\omega_t, \omega_\tau) = (E_m - E_p, -E_n)$.

As discussed in the main text, the grid of discrete peaks at $(E_m, -E_n)$ has two distinct contributions, the $R_2 = R_3$ process with the intermediate state $|Q\rangle$ being the ground state [Fig. 18(b)], and the R_1 contribution from the process where a new domain is created at a different location [Fig. 18(d)]. In the latter case, the four-kink states form a continuum, as only their total momentum is fixed, which leads to the continuous negative features appearing to the right of each $(E_m, -E_n)$ peak.

A single spin flip can create a four-kink (or two domain) state from a two-kink (or one domain) state with a domain length of $l = n$. For $n \geq 3$, this can occur by splitting the existing domain into two. Depending on how many spins are flipped and which ones, several two-domain configurations are possible. For example, from a domain of length $l = 5$, we can create two $l_{1/2} = 2$ domains or a pair of $l_1 = 1$ and $l_2 = 3$ domains by flipping a single spin. The four-kink state with $l_1 = 1$ and $l_2 = n - 2$ generally have the lowest energy among possible configurations with $l_1 + l_2 = n - 1$. The contribution from such a domain splitting process appears at $(E_1 - [E_n - E_{n-2}], -E_n)$ in the case of a single spin flip, as indicated by the extended green arrows in Fig. 18(e). Just as in the process involving adding a second domain, the four-kink state created by the domain splitting process form a continuum. Since each state in the continuum has a higher energy than $E_1 + E_{n-2}$, the continuum appears to the right side of $(E_1 - [E_n - E_{n-2}], -E_n)$. As the spacing $E_n - E_{n-2}$ decreases with increasing n , the signal from the domain splitting process becomes squeezed closer to $(E_1, -E_n)$ for larger n .

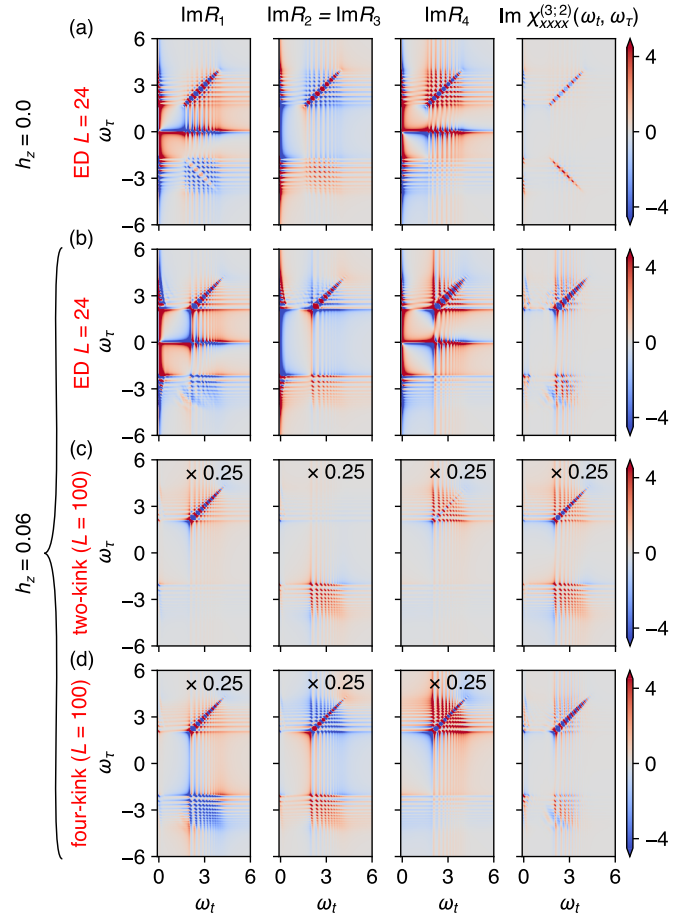


FIG. 19. Separate calculation of each R_a using ED [(a), (b)], the two-kink approximation (c), and the four-kink approximation (d). When $t_1 = \tau, t_2 = 0$, and $t_3 = t$, $R_2 = R_3$ applies. Parameters used are $J = 0.7$ and $h_x = 0.3$.

For $n \geq 4$, a four-kink state can also be created by flipping two neighboring spins to split the domain into two. The lowest energy is again given by the configuration with $l_1 = 1$ and $l_2 = n - 3$ domains, resulting in a continuous signal starting from $(E_1 - [E_n - E_{n-3}], -E_n)$. In Fig. 18(e), this signal gives rise to positive poles, indicated by the extended pink arrows. It is also possible to create four-kink states by flipping more and more spins, requiring a larger and larger domain size, which produces a sign-alternating sequence of continuous line features in the 2DCS, with the sign depending on the parity of the number of spin flips.

APPENDIX G: SEPARATE CALCULATION OF EACH R_a

In the main text, we numerically apply a magnetic field in a manner similar to the MPS study in Ref. [21]. Alternatively, we can directly calculate the imaginary part of R_a using ED, which is more similar to the technique used in Ref. [22]. Even though each R_a is not accessible by experiment, it can be useful to understand which processes contribute to each signal. Here we provide an example in Fig. 19 where we calculate the imaginary part of each R_a using ED and the two/four-kink approximation.

Figure 19(a) shows the case of $h_z = 0.0$, i.e., the exactly solvable case. In addition to the peaks in $\chi_{xxxx}^{(3;2)}$, we observe additional signals along the $\omega_t = 0$ and $\omega_\tau = 0$ axes. These exist due to the finite value of m_{00}^x , which arises from the finite value of h_x . However, these contributions cancel each other out, giving zero intensity once the sum of R_a is taken. Another feature is that, in addition to the antidiagonal rephasing signal, we find off-diagonal rephasing signals of opposite sign in R_1 and $R_2 = R_3$. The former comes from the process where the intermediate state $|Q\rangle$ is a ground state [Fig. 18(b)], while the latter comes from the process where $|Q\rangle$ is a four-kink state [Fig. 18(d)]. The noninteracting nature of the two pairs of kinks makes the complete cancellation of R_1 and $2R_2$ possible. An exception is when $k_1 = k_2$, in which case the creation of the second pair of kinks is forbidden due to the fermionic statistics of the spinons, which explains the absence of peaks at $\omega_t = -\omega_\tau$ in R_1 . After taking the sum of $R_1 + 2R_2 + R_4$, we

recover the correct signal, without the off-diagonal rephasing signals.

As discussed in the main text, for finite h_z , the spinons interact with each other, leading to a partial cancellation of off-diagonal peaks between R_1 and R_2 [Fig. 19(b)]. In the two-kink approximation [Fig. 19(c)], we do not observe any rephasing signals in R_1 , confirming that the rephasing signal in R_1 originates from processes where the intermediate state $|Q\rangle$ is a four-kink state. It is important to note that each R_a contains extensive terms, which results in the signal strength of the two-/four-kink approximation calculated for $L = 100$ being much stronger than the ED data for $L = 24$. If the signal cancellation occurs properly, the sum of R_a should be independent of the system size, which is not the case for the two-kink approximation. Additionally, since m_{00}^x is zero in the two-/four-kink approximation, we do not observe the additional signals along the $\omega_\tau = 0$ axis.

-
- [1] T. Kampfrath, A. Sell, G. Klatt, A. Pashkin, S. Mährlein, T. Dekorsy, M. Wolf, M. Fiebig, A. Leitenstorfer, and R. Huber, Coherent terahertz control of antiferromagnetic spin waves, *Nat. Photonics* **5**, 31 (2011).
- [2] C. M. Morris, R. Valdés Aguilar, A. Ghosh, S. M. Koohpayeh, J. Krizan, R. J. Cava, O. Tchernyshyov, T. M. McQueen, and N. P. Armitage, Hierarchy of bound states in the one-dimensional ferromagnetic ising chain CoNb_2O_6 investigated by high-resolution time-domain terahertz spectroscopy, *Phys. Rev. Lett.* **112**, 137403 (2014).
- [3] X. Zhang, F. Mahmood, M. Daum, Z. Dun, J. A. M. Paddison, N. J. Laurita, T. Hong, H. Zhou, N. P. Armitage, and M. Mourigal, Hierarchy of exchange interactions in the triangular-lattice spin liquid YbMgGaO_4 , *Phys. Rev. X* **8**, 031001 (2018).
- [4] A. Bera, S. Bera, S. Kalimuddin, S. Gayen, M. Kundu, B. Das, and M. Mondal, Review of recent progress on THz spectroscopy of quantum materials: superconductors, magnetic and topological materials, *Eur. Phys. J.: Spec. Top.* **230**, 4113 (2021).
- [5] T.-H. Han, J. S. Helton, S. Chu, D. G. Nocera, J. A. Rodriguez-Rivera, C. Broholm, and Y. S. Lee, Fractionalized excitations in the spin-liquid state of a kagome-lattice antiferromagnet, *Nature (London)* **492**, 406 (2012).
- [6] M. Mourigal, M. Enderle, A. Klöpperpieper, J.-S. Caux, A. Stunault, and H. M. Rønnow, Fractional spinon excitations in the quantum Heisenberg antiferromagnetic chain, *Nat. Phys.* **9**, 435 (2013).
- [7] J. Wen, S.-L. Yu, S. Li, W. Yu, and J.-X. Li, Experimental identification of quantum spin liquids, *npj Quantum Mater.* **4**, 12 (2019).
- [8] A. Banerjee, C. A. Bridges, J.-Q. Yan, A. A. Aczel, L. Li, M. B. Stone, G. E. Granroth, M. D. Lumsden, Y. Yiu, J. Knolle, S. Bhattacharjee, D. L. Kovrizhin, R. Moessner, D. A. Tennant, D. G. Mandrus, and S. E. Nagler, Proximate Kitaev quantum spin liquid behaviour in a honeycomb magnet, *Nat. Mater.* **15**, 733 (2016).
- [9] Z. Zhu, P. A. Maksimov, S. R. White, and A. L. Chernyshev, Disorder-induced mimicry of a spin liquid in YbMgGaO_4 , *Phys. Rev. Lett.* **119**, 157201 (2017).
- [10] Y. Shen, Y.-D. Li, H. Wo, Y. Li, S. Shen, B. Pan, Q. Wang, H. C. Walker, P. Steffens, M. Boehm, Y. Hao, D. L. Quintero-Castro, L. W. Harriger, M. D. Frontzek, L. Hao, S. Meng, Q. Zhang, G. Chen, and J. Zhao, Evidence for a spinon Fermi surface in a triangular-lattice quantum-spin-liquid candidate, *Nature (London)* **540**, 559 (2016).
- [11] I. Kimchi, A. Nahum, and T. Senthil, Valence bonds in random quantum magnets: Theory and application to YbMgGaO_4 , *Phys. Rev. X* **8**, 031028 (2018).
- [12] Z. Ma, J. Wang, Z.-Y. Dong, J. Zhang, S. Li, S.-H. Zheng, Y. Yu, W. Wang, L. Che, K. Ran, S. Bao, Z. Cai, P. Čermák, A. Schneidewind, S. Yano, J. S. Gardner, X. Lu, S.-L. Yu, J.-M. Liu, S. Li *et al.*, Spin-glass ground state in a triangular-lattice compound YbZnGaO_4 , *Phys. Rev. Lett.* **120**, 087201 (2018).
- [13] J. Lu, X. Li, H. Y. Hwang, B. K. Ofori-Okai, T. Kurihara, T. Suemoto, and K. A. Nelson, Coherent two-dimensional terahertz magnetic resonance spectroscopy of collective spin waves, *Phys. Rev. Lett.* **118**, 207204 (2017).
- [14] Z. Zhang, F. Y. Gao, J. B. Curtis, Z.-J. Liu, Y.-C. Chien, A. von Hoegen, T. Kurihara, T. Suemoto, P. Narang, E. Baldini, and K. A. Nelson, Three-wave mixing of anharmonically coupled magnons, *Nat. Phys.* **20**, 801 (2024).
- [15] Z. Zhang, F. Y. Gao, Y.-C. Chien, Z.-J. Liu, J. B. Curtis, E. R. Sung, X. Ma, W. Ren, S. Cao, P. Narang, A. von Hoegen, E. Baldini, and K. A. Nelson, Terahertz-field-driven magnon upconversion in an antiferromagnet, *Nat. Phys.* **20**, 788 (2024).
- [16] M. Khalil, N. Demirdöven, and A. Tokmakoff, Coherent 2D IR spectroscopy: Molecular structure and dynamics in solution, *J. Phys. Chem. A* **107**, 5258 (2003).
- [17] S. T. Cundiff, A. D. Bristow, M. Siemens, H. Li, G. Moody, D. Karaickaj, X. Dai, and T. Zhang, Optical 2-D fourier transform spectroscopy of excitons in semiconductor nanostructures, *IEEE J. Sel. Top. Quantum Electron.* **18**, 318 (2012).
- [18] M. Fava, S. Gopalakrishnan, R. Vasseur, F. H. L. Essler, and S. A. Parameswaran, Divergent nonlinear response from quasi-particle interactions, *Phys. Rev. Lett.* **131**, 256505 (2023).
- [19] Y. Wan and N. P. Armitage, Resolving continua of fractional excitations by spinon echo in THz 2D coherent spectroscopy, *Phys. Rev. Lett.* **122**, 257401 (2019).

- [20] Z.-L. Li, M. Oshikawa, and Y. Wan, Photon echo from lensing of fractional excitations in Tomonaga-Luttinger spin liquid, *Phys. Rev. X* **11**, 031035 (2021).
- [21] Q. Gao, Y. Liu, H. Liao, and Y. Wan, Two-dimensional coherent spectrum of interacting spinons from matrix product states, *Phys. Rev. B* **107**, 165121 (2023).
- [22] G. Sim, J. Knolle, and F. Pollmann, Nonlinear spectroscopy of bound states in perturbed Ising spin chains, *Phys. Rev. B* **107**, L100404 (2023).
- [23] G. Sim, F. Pollmann, and J. Knolle, Microscopic details of two-dimensional spectroscopy of one-dimensional quantum Ising magnets, *Phys. Rev. B* **108**, 134423 (2023).
- [24] M. Potts, R. Moessner, and O. Benton, Exploiting polarization dependence in two dimensional coherent spectroscopy: examples of $\text{Ce}_2\text{Zr}_2\text{O}_7$ and $\text{Nd}_2\text{Zr}_2\text{O}_7$, *Phys. Rev. B* **109**, 104435 (2024).
- [25] O. Hart and R. Nandkishore, Extracting spinon self-energies from two-dimensional coherent spectroscopy, *Phys. Rev. B* **107**, 205143 (2023).
- [26] R. M. Nandkishore, W. Choi, and Y. B. Kim, Spectroscopic fingerprints of gapped quantum spin liquids, both conventional and fractonic, *Phys. Rev. Res.* **3**, 013254 (2021).
- [27] W. Choi, K. H. Lee, and Y. B. Kim, Theory of two-dimensional nonlinear spectroscopy for the Kitaev spin liquid, *Phys. Rev. Lett.* **124**, 117205 (2020).
- [28] Y. Qiang, V. L. Quito, T. V. Trevisan, and P. P. Orth, Probing Majorana wave functions in Kitaev honeycomb spin liquids with second-order two-dimensional spectroscopy, *Phys. Rev. Lett.* **133**, 126505 (2024).
- [29] M. K. Negahdari and A. Langari, Nonlinear response of the Kitaev honeycomb lattice model in a weak magnetic field, *Phys. Rev. B* **107**, 134404 (2023).
- [30] M. McGinley, M. Fava, and S. A. Parameswaran, Signatures of fractional statistics in nonlinear pump-probe spectroscopy, *Phys. Rev. Lett.* **132**, 066702 (2024).
- [31] U. Schollwöck, The density-matrix renormalization group in the age of matrix product states, *Ann. Phys.* **326**, 96 (2011), January 2011 Special Issue.
- [32] S. Mukamel, *Principles of Nonlinear Optical Spectroscopy*, Oxford series in optical and imaging sciences (Oxford University Press, Oxford, 1995).
- [33] W. Kuehn, K. Reimann, M. Woerner, T. Elsaesser, and R. Hey, Two-dimensional terahertz correlation spectra of electronic excitations in semiconductor quantum wells, *J. Phys. Chem. B* **115**, 5448 (2011).
- [34] R. B. Sidje, Expokit: a software package for computing matrix exponentials, *ACM Trans. Math. Softw.* **24**, 130 (1998).
- [35] S. Sugiura and A. Shimizu, Thermal pure quantum states at finite temperature, *Phys. Rev. Lett.* **108**, 240401 (2012).
- [36] S. Sugiura and A. Shimizu, Canonical thermal pure quantum state, *Phys. Rev. Lett.* **111**, 010401 (2013).
- [37] S. B. Rutkevich, On the weak confinement of kinks in the one-dimensional quantum ferromagnet CoNb_2O_6 , *J. Stat. Mech.* (2010) P07015.
- [38] R. Coldea, D. A. Tennant, E. M. Wheeler, E. Wawrzynska, D. Prabhakaran, M. Telling, K. Habicht, P. Smeibidl, and K. Kiefer, Quantum criticality in an Ising chain: Experimental evidence for emergent E_8 symmetry, *Science* **327**, 177 (2010).
- [39] G. Zhang and Z. Song, Topological characterization of extended quantum Ising models, *Phys. Rev. Lett.* **115**, 177204 (2015).
- [40] W.-L. You, Y.-C. Qiu, and A. M. Oleś, Quantum phase transitions in a generalized compass chain with three-site interactions, *Phys. Rev. B* **93**, 214417 (2016).
- [41] C. M. Morris, N. Desai, J. Viirik, D. Hüvonen, U. Nagel, T. Rõõm, J. W. Krizan, R. J. Cava, T. M. McQueen, S. M. Koohpayeh, R. K. Kaul, and N. P. Armitage, Duality and domain wall dynamics in a twisted Kitaev chain, *Nat. Phys.* **17**, 832 (2021).
- [42] H. M. Babujian, M. Karowski, and A. M. Tsvelik, Probing strong correlations with light scattering: Example of the quantum Ising model, *Phys. Rev. B* **94**, 155156 (2016).
- [43] H. Babujian, M. Karowski, and A. Tsvelik, Multipoint green's functions in 1+1 dimensional integrable quantum field theories, *Nucl. Phys. B* **917**, 122 (2017).
- [44] S. Rutkevich, Energy spectrum of bound-spinons in the quantum Ising spin-chain ferromagnet, *J. Stat. Phys.* **131**, 917 (2008).
- [45] S. Birnkammer, A. Bastianello, and M. Knap, Prethermalization in one-dimensional quantum many-body systems with confinement, *Nat. Commun.* **13**, 7663 (2022).
- [46] J. Vovrosh, R. Mukherjee, A. Bastianello, and J. Knolle, Dynamical hadron formation in long-range interacting quantum spin chains, *PRX Quantum* **3**, 040309 (2022).
- [47] M. Fava, R. Coldea, and S. A. Parameswaran, Glide symmetry breaking and Ising criticality in the quasi-1D magnet CoNb_2O_6 , *Proc. Natl. Acad. Sci. USA* **117**, 25219 (2020).
- [48] Y. Watanabe, S. Trebst, and C. Hickey, Data and code for "Exploring two-dimensional coherent spectroscopy with exact diagonalization spinons and confinement in 1D quantum magnets", Zenodo, doi:10.5281/zenodo.10636275 (2024).
- [49] T. Iitaka and T. Ebisuzaki, Algorithm for linear response functions at finite temperatures: Application to ESR spectrum of $s = \frac{1}{2}$ antiferromagnet Cu benzoate, *Phys. Rev. Lett.* **90**, 047203 (2003).